© 2018. Published by The Company of Biologists Ltd | Development (2018) 145, dev160879. doi:10.1242/dev.160879

TECHNIQUES AND RESOURCES

RESEARCH ARTICLE

A targeted 3D EM and correlative microscopy method using SEM array tomography

Agnes Burel[1], Marie-Thérèse Lavault[1], Clément Chevalier[1,*], Helmut Gnaegi[2], Sylvain Prigent[1], Antonio Mucciolo[3], Stéphanie Dutertre[1], Bruno M. Humbel[3], Thierry Guillaudeux[1] and Irina Kolotuev[1,3,‡]

ABSTRACT

Using electron microscopy to localize rare cellular events or structures in complex tissue is challenging. Correlative light and electron microscopy procedures have been developed to link fluorescent protein expression with ultrastructural resolution. Here, we present an optimized scanning electron microscopy (SEM) workflow for volumetric array tomography for asymmetric samples and model organisms (*Caenorhabditis elegans*, *Drosophila melanogaster*, *Danio rerio*). We modified a diamond knife to simplify serial section array acquisition with minimal artifacts. After array acquisition, the arrays were transferred to a glass coverslip or silicon wafer support. Using light microscopy, the arrays were screened rapidly for initial recognition of global anatomical features (organs or body traits). Then, using SEM, an in-depth study of the cells and/or organs of interest was performed. Our manual and automatic data acquisition strategies make 3D data acquisition and correlation simpler and more precise than alternative methods. This method can be used to address questions in cell and developmental biology that require the efficient identification of a labeled cell or organelle.

KEY WORDS: Correlative light and electron microscopy (CLEM), Array tomography, Volume reconstruction, Model organisms, *C. elegans*, *Drosophila*

INTRODUCTION

Imaging methods aid the analysis and understanding of biological processes. Advanced fluorescent light microscopy (FLM) techniques can answer questions about the localization, dynamics and interactions of proteins in various organs and cell structures. Genetically encoded fluorescence tools enable the study of live processes. However, many cellular processes cannot be fully visualized, because of the insufficient resolution of fluorescence labeling and the lack of visible reference structures within the cell. Much higher resolution of cellular components can be obtained with electron microscopy (EM), which is crucial for the analysis of cellular ultrastructure. Recently, cellular ultrastructure has been directly correlated with a fluorescence signal using correlative light and electron microscopy (CLEM; Caplan et al., 2011; Muller-Reichert and Verkade, 2014).

[1]University of Rennes 1, UMS Biosit, MRic, 35043 Rennes, France. [2]Diatome SA, Helmstrasse 1, 2560 Nidau, Switzerland. [3]University of Lausanne, Faculté de biologie et de médecine, Electron Microscopy Facility, CH-1015 Lausanne, Switzerland.
*Present address: ULB, Center for Microscopy and Molecular Imaging, B-6041 Gosselies, Belgium.

‡Author for correspondence (irina.kolotueva@unil.ch)

I.K., 0000-0001-6251-5155

Received 25 October 2017; Accepted 16 May 2018

Serial section transmission electron microscopy (TEM), and tilt series combined with electron tomography, have been the primary tools for reconstructing ultrastructure within a defined volume. These methods have contributed significantly to our current understanding of the local 3D organization of biological samples (White et al., 1986; Bumbarger et al., 2007; Noske et al., 2008; Anderson et al., 2011; Saalfeld et al., 2012; Bock et al., 2011; Doroquez et al., 2014; Lee et al., 2016). Unfortunately, these procedures require a high level of training and are both time-consuming and prone to occasional loss of sections, resulting in loss of information. Recently developed alternative methods for serial sectioning, such as serial block face scanning electron microscopy (SBFSEM) and focused ion beam scanning electron microscopy (FIB-SEM), which use back-scattered electrons to image the block surface, have helped to address biological questions that require the analysis of large EM volumes (Denk and Horstmann, 2004; Heymann et al., 2006; Knott et al., 2011; Kizilyaprak et al., 2014; Titze and Genoud, 2016). During these approaches, the block surface is imaged, and then sections are removed. The new block surface is then imaged again. This cyclical repetition results in the generation of an automatically aligned stack of numerous sections. Although these approaches result in efficient 3D data acquisition, re-imaging the same sample at another region of interest or at a different resolution is impossible, as is on-section immunolabeling or post-staining contrast enhancement with heavy metals. These problems can be overcome, as has been shown in several studies that correlated light and FIB-SEM data on cells in culture, in brain tissue and in developing blood vessels in zebrafish (Bushby et al., 2012; Lucas et al., 2012, 2014; Maco et al., 2013; Bosch et al., 2015; Blazquez-Llorca et al., 2015). Notably, such elegant studies require rare and expensive equipment, available only in specialized labs with limited external access.

Array tomography (AT) was developed by Micheva and collaborators to study protein localization in synapses (Micheva and Smith, 2007; Micheva et al., 2010; Collman et al., 2015). The samples are embedded in a hydrophilic resin and sectioned into long ribbons of serial sections (the arrays) using an ultramicrotome. The sections are then transferred to a glass coverslip (instead of a microscope grid) and analyzed by light microscopy followed by scanning electron microscopy (SEM). To localize a large number of proteins in a single series of sections, several rounds of fluorescence labeling are performed, using antibodies combined with an antibody elution step before each additional round. The EM-like sample preparation procedure enables analysis of the cellular ultrastructure with the localization of a fluorescence signal.

AT is used in different procedures, depending on the research goal. (1) Multiplex FLM is used to detect numerous fluorophores (Table 1, Multiplex labeling). The mild sample treatment and hydrophilic resin embedding usually compromises the quality of the ultrastructure. (2) Serial EM is used for volume acquisition and

Development (2018) 145, dev160879. doi:10.1242/dev.160879

Table 1. A simplified summary of AT procedures with the changes in the flow necessary for three preparation strategies

Steps	Multiplex labeling	Volume reconstruction	CLEM
Fixation	HPF-QFS	OTO	HPF-QFS
Embedding resin	Acrylic	Epon	Acrylic
Sectioning and transfer	Coverslip	Silicon wafer	Coverslip or silicon wafer
Stain	Primary and secondary antibodies	Direct observation	Direct observation or primary and secondary antibodies
Microscope type	Wide-field/confocal	FEG-SEM	Wide-field /confocal FEG-SEM
Destaining	0.2 M NaOH, 0.02% SDS	NA	NA
Restain	Primary and secondary antibodies		UAc/Pb
Reconstruction	Fiji/3Dmod		

FEG-SEM, field emission gun scanning electron microscopy; HPF-QFS, high-pressure freezing-quick freeze substitution; NA, not applicable; OTO, enhanced contrast procedure; UAc/Pb, UAc/Sato's Pb staining.

After fixation, the embedding medium differs: hydrophilic acrylic resin is preferred when there is a need to preserve antigenicity and fluorescence signals; hydrophobic epoxy resins are used when the ultrastructure is the main goal. The microscope used depends on the imaging goal.

region of interest (ROI) recognition, when ultrastructural preservation is crucial (Table 1, Volume reconstruction). As the back-scattered SEM mode is used, high contrast with multiple heavy metal stains is required. This preparation uses standard or enhanced contrast TEM with epoxy resin-based embedding. (3) Correlative fluorescence EM is used to preserve fluorescence and ultrastructure quality, both *en bloc* and on section (Table 1, CLEM). Freeze-substitution with acrylic resin embedding can provide efficient fluorescence retention (Nixon et al., 2009; Kukulski et al., 2011; Watanabe et al., 2011; Peddie et al., 2014; McDonald, 2014; Burette et al., 2015; Kremer et al., 2015; Paez-Segala et al., 2015; this study). However, the retention of the fluorescence signal with this approach is unpredictable and largely dependent on the specific fluorescent fusion protein used.

Although AT is a powerful technique, its use has been predominantly restricted to addressing questions in neurobiology, for which it was developed (Oberti et al., 2011). Recent studies have applied AT to other fields (Jahn et al., 2016; Markert et al., 2016). For AT, sections are cut and transferred to a solid support, such as a coverslip, an indium-tin oxide-coated coverslip, a silicon wafer or a Kapton plastic tape (Micheva and Smith, 2007; Pluk et al., 2009; Kasthuri et al., 2015) using special slide/wafer retraction mechanisms (Wacker and Schroeder, 2013; Hayworth et al., 2014). AT-SEM is increasingly used as an alternative to TEM serial section SBF and FIB-SEM imaging methods to analyze large surface areas in a non-destructive manner. It allows the direct 3D correlation of CLEM samples with both fluorescence and electron microscopy data. Unlike other volume sections transferred to a solid support, these samples can be stored, re-imaged multiple times, and even re-contrasted with heavy metals to improve the signal-to-noise ratio (Schwarz and Humbel, 2014).

Large volume data analysis is required to answer some biological questions. Other questions can be answered by analyzing limited volumes from numerous independent samples or events. To provide a method to answer these questions that is accessible to the wider scientific community, without technical limitations, we have modified and adapted the AT technique. Our method encompasses the entire procedure from sample preparation to data analysis. We transfer serial sections to glass coverslips or silicon wafers (hereafter referred to as 'wafer'), label with heavy metals and use high-resolution volume FLM and EM. We have optimized sample preparation, configured a diamond knife to facilitate the transfer of sections to support and devised an efficient sectional screening strategy. This method can be used with a variety of model organisms. It does not require additional expensive equipment beyond that of most modern research facilities. To demonstrate our technique, we analyzed both *Caenorhabditis elegans* and *Drosophila melanogaster*.

RESULTS

Sample preparation methods and sectioning strategy

When analyzing polarized samples and small model organisms, the relevant cellular structure, or ROI, can be located using the known morphology and anatomy of the tissue as landmarks. The principal problem with these complex samples is that only one ROI may be present in each sample. Because imaging only one individual structure would be insufficient to make a statistically significant observation, numerous samples must be analyzed.

Our strategy to efficiently localize the ROI in a single sample includes two-step flat embedding, precise block trimming (Fig. 1A,B; Kolotuev, 2014) and serial sectioning. We use light microscopy to locate the ROI rapidly for subsequent EM analysis, precisely orient the sample, and delimit the area for ultra-thin sectioning. To optimize the stability of the ribbon of consecutive sections, we remove the excess embedding resin surrounding the sample. With homogeneous tissue, excess embedding resin can be easily trimmed away from a sample (referred to as 'tight trimming'). With non-homogeneous tissue, such as *C. elegans* or *Drosophila*, even 'tight trimming' cannot entirely remove the excess resin. Thus, we use our trimming diamond tool for 'tight trimming' to leave a minimal amount of excess resin around the sample. To acquire long ribbons of consecutive sections (>300 sections), we prefer to shape the surface of the block to a rectangle, with the edge parallel to the knife, such that the block length measures twice the length of the side edges. A larger sectional surface tends to produce more folds, whereas sections with a smaller surface tend to curl.

To produce horizontally aligned sections on support (glass coverslips or wafers), we use a modified diamond knife that greatly facilitates the efficient generation of long ribbons of consecutive sections (Fig. 1C-H; see detailed description below). Left intact, these long ribbons can complicate subsequent manual data acquisition: without obvious structural variation, mistakes will often be made during the monotonous analysis of long ribbons of consecutive sections. Thus, for our rapid screening approach, we carefully subdivide the long ribbons initially produced into shorter ribbons of consecutive sections (50-100 sections), and then horizontally align the shorter ribbons alongside each other, in rows, on the support. This way, ten short ribbons (i.e. more than 500 sections) can be easily aligned on a small support, be it a coverslip or a wafer (Fig. 1H). Then, instead of thoroughly analyzing every section within a long ribbon in a serial 'vertical' fashion (from 0 to 100+), we 'leap' between centrally located sections across the short

Development (2018) 145, dev160879. doi:10.1242/dev.160879

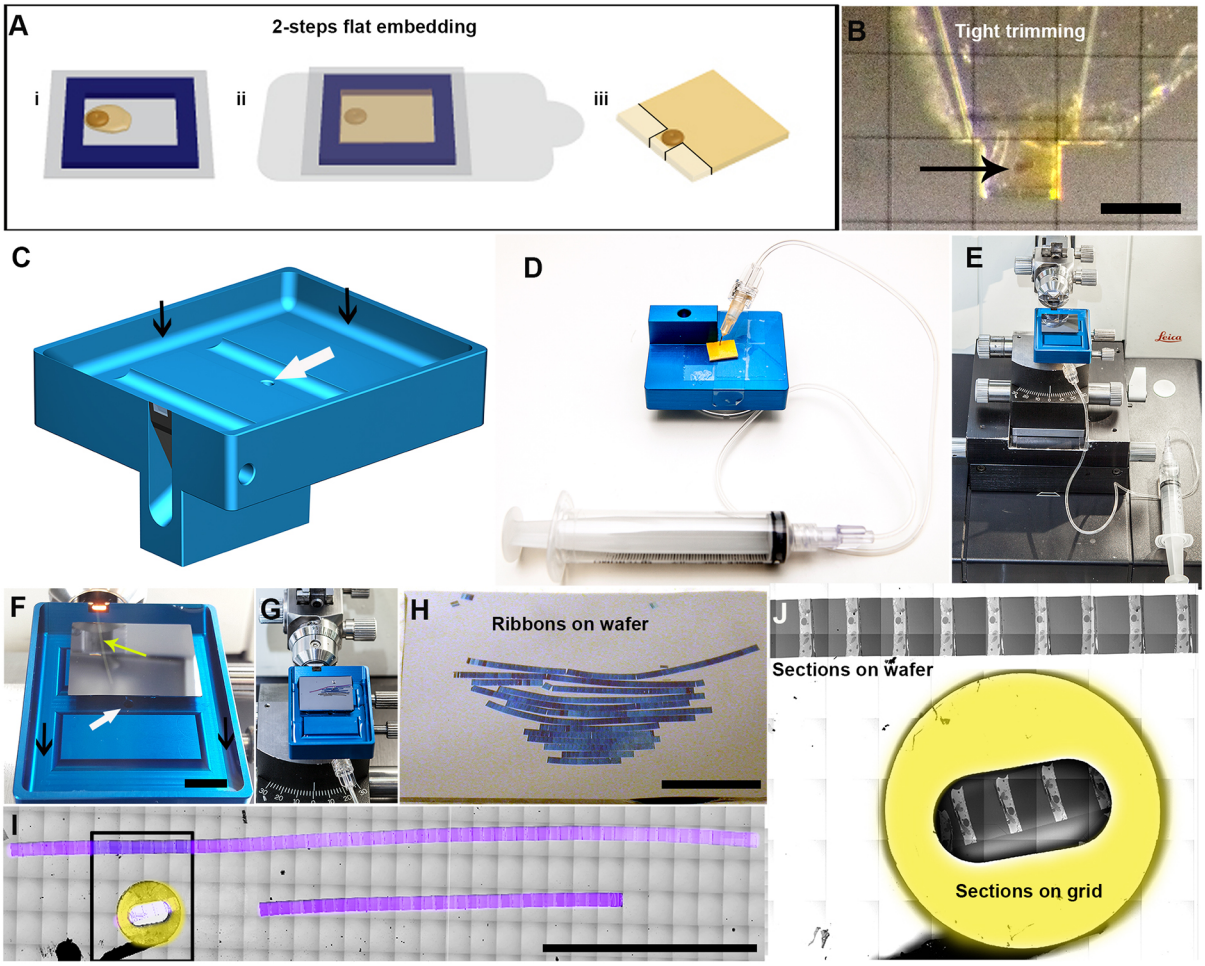

Fig. 1. AT: generation of arrays of aligned ribbons of consecutive sections. (A) Two-step flat embedding procedure: Resin-infiltrated samples are pre-polymerized on the film within a frame (i). Next, the frame is filled with resin and set to polymerize completely (ii). These flat blocks can be directly sectioned without further re-embedding, allowing rapid localization of the samples. Black lines outlining the bright zones show the area dedicated for the trimming (iii). (B) Tight trimming of the sample with the 90° diamond trim knife: The sample is oriented in the middle of resin support (arrow) and the surrounding resin tightly trimmed. This minimizes the amount of resin around the sample, reducing the surface area of each section, and maximizing the number of sections that can be accommodated on one microscope slide or wafer. (C) A drawing of a modified AT-boat diamond knife enlarged and flattened to facilitate sectional collection on glass or wafer support. As part of the modifications, we carved water evacuation ditches (black arrows) and drilled a hole (white arrow) in the bottom of the boat. (D) A syringe needle is connected to the hole and covered with double-sided sticky tape. A catheter tube connects it to a syringe. The internal diameter of the needle determines the speed of water retraction. Thus, water can be retracted, or drained, from below the water surface, either actively, using the syringe, or passively, by allowing water to drip at a steady pace through the catheter, leaving both hands of the operator free to align sections on the support. (E) A complete setup for array generation: the modified AT diamond knife is connected to a syringe and installed on the ultramicrotome. Before sectioning, the support (a coverslip or wafer) is entirely submerged in water and lies parallel to the water surface. (F) A ribbon of consecutive sections floating inside the modified boat while sectioning (green arrow). A rectangular wafer lies on the bottom of the boat (black arrows indicate water evacuation ditches; white arrow indicates hole in the bottom of the boat). (G) After sectioning, the ribbons of consecutive sections are aligned side by side, and water is gradually drained from the boat. After either assisting with a syringe or allowing the water to drain away completely, the support remains at the bottom of the boat until any remaining moisture has evaporated completely from its surface (Movie 1). (H) Aligned ribbons of consecutive sections transferred to wafer support. (I) A stitched montage of multiple light microscopy images acquired with the CorrSight, showing 115 sections (pseudo colored in purple) on a wafer versus three on the TEM grid (yellow circle). (J) Magnification of the boxed area in I showing the stitched SEM images acquired with the MAPs interface covering part of the wafer, and a TEM grid with the sections from the same preparation (yellow circle). Scale bars: 200 µm in B; 1 cm in F,H; 10 mm in I,J.

horizontally aligned ribbons to screen visually for the ROI (see detailed example below).

Sequential section analysis using TEM grids is very tedious and numerous problems can emerge. If the sectional surface is relatively large, then very few sections will fit on one grid. If multiple sections do fit on one grid, then sample collection is error-prone because of the risk of sectional loss. Data analysis is also very time consuming because each section on the grid must be manually screened to find the ROI and orient the sample. For serial section collection, even a relatively short sequence of sections (e.g. 100) transferred to support (glass coverslips or wafers) presents significant advantages compared with sections on TEM grids (Fig. 1I,J). On support, 115 serial sections can be analyzed in less than 15 min after orienting the trimmed block optimally relative to the AT knife. Analysis of 115 sections on TEM grids would require much more time and result in significantly less precise data. For any scientific question that needs a resolution compatible with FIB-SEM and SBFSEM, our transfer technique has clear benefits over serial section TEM.

Modified diamond knife

Both the histo and the ultra jumbo diamond knives (Diatome) hold a coverslip in their large boat at an optimal angle for collecting

Development (2018) 145, dev160879. doi:10.1242/dev.160879

semi-thin sections. These knives can be used to generate arrays of sections, i.e. long ribbons of consecutive sections. In the published AT procedure, the array of sections is moved to the rear edge of the coverslip where it touches the interface between the glass and the water (Micheva and Smith, 2007). To attach the sections to support, water is drained from the side of the knife boat using a syringe (Micheva and Smith, 2007), or the coverslip is pulled out of the trough using a micromanipulator (Horstmann et al., 2012; Wacker et al., 2016). In our hands, this method compromises the control of water during draining. The resulting rapid drying of the sections on support can create wrinkles or folds in the sections and cause ROIs to be lost from view.

We have developed a water-draining system for the histo jumbo diamond knife, which reduces the incidence of sectional folding and wrinkling, and we have modified the diamond knife to better suit AT: (1) We replaced the diamond blade for the histo jumbo diamond knife for semi-thin sectioning (~500 nm) with the diamond blade for the ultra 35° knife for cutting ultra-thin sections (~50 nm). Ultra-thin sections have better quality than semi-thin sections: unlike semi-thin sections, ultra-thin AT sections with a thickness of 50-100 nm give better *z*-resolution and generate fewer folds. Ultra-thin sections also improve the quality of subsequent analysis, as they adhere better to the support and provide higher ultrastructural resolution. (2) We increased the size of the knife boat to completely accommodate a coverslip on a flat support on the bottom of the trough at a 0° angle. The support for the coverslip is surrounded with a ditch to allow for user-controlled water draining. A hole in the bottom of the boat facilitates the insertion of a flexible tube attached to a syringe (Fig. 1C,D). Using the syringe, water can be added to or retracted from the boat without creating turbulence, which had presented problems while using previous methods (Fig. 1E). To attach the sections to support, water is drained slowly through the hole in the bottom of the boat. Slow water removal avoids turbulence and allows the sections to dry slowly, without wrinkles and folds.

This technique of attaching the section ribbons to support is the same for all types of support. After generating the ribbon of the desired length (Fig. 1F), the water level in the boat is gradually lowered, by draining the water slowly through the hole in the bottom of the boat, either actively, by aspiration with the syringe, or passively, by allowing the water to drip through the tube without a syringe attached to it (Fig. 1G). When the water level reaches the height of the transfer support, the sections are manually aligned and arranged side by side (Fig. 1G,H, Movie 1). In our experience, this method greatly facilitates the ease and accuracy of section transfer for CLEM and volume EM. The same principle can also be used to collect histological sections for light microscopy analysis.

Multiplex immunolabeling

The immunolocalization of antigens is compromised by low *z*-resolution for both standard and super-resolution light microscopy. Also, the colocalization of multiple antigens using antibodies generated in the same species is often problematic. The advantage of AT is that sections can be cut as thin as 40 nm, and images of several cycles of immunofluorescence labeling can be acquired individually, and then superimposed. Physical ultra-thin sectioning can achieve a *z*-resolution of a few tens of nanometers, which is an order of magnitude better than the *z*-resolution of currently available super-resolution microscopes.

C. elegans is a transparent worm, which makes it an ideal model organism for light microscopy. Unfortunately, most specific primary antibodies available for *C. elegans* research are either mouse monoclonal or rabbit polyclonal. Thus, the colocalization of multiple antibodies on the same sections is often impossible. To demonstrate the power of the AT approach, we labeled serial sections of *C. elegans* larvae prepared by high-pressure freezing-freeze substitution (HPF-FS; see the Materials and Methods sample preparation section for details) on coverslip support. We stained/labeled the arrays of 100 nm thick sections with DAPI (nuclei, blue), anti-tubulin (red) and anti-ERM1 (EB1, green) in the first cycle and, after destaining, we stained for DAPI, anti-actin (red) and anti-VHA5 (green) in the second cycle (Fig. 2A,B). Both rounds of immunolabeling gave a strong signal, equally visible on individual sections and on the merge of all 25 sections (Fig. 2A,B, Movie 2). Before relabeling and re-analyzing the samples, we extensively washed the sections between the labeling cycles, and verified that the previous labeling had been completely removed. We used the manual acquisition of the images, improved their alignment by developing a new Fiji macro, and superimposed all markers in one data set (Fig. 2C). DAPI nuclear staining served as a useful reference marker to facilitate the alignment of the complementary signals provided by the two independent labeling cycles.

To monitor the quality and feasibility of EM acquisition, and to correlate the labeling data on sections after two labeling cycles, we imaged the corresponding ROIs with SEM using the back-scattered electron (BSE) detector. The fluorescence signal could be identified quickly, and the overall ultrastructure was well preserved (Fig. 2D). To improve the accuracy of superposition, we used DAPI nuclear staining and examined the nuclear ultrastructure and other structural features of the sample (Fig. 2E).

Localization of ROI and volume reconstruction

In complex tissues, drawing conclusions about the ultrastructure from a single section or a small number of sections can be impossible. Volume reconstruction of cells and tissues using the SBF and FIB-SEM methods is an efficient way to investigate the relationship between cells and organelles in their complex 3D cellular context. For both approaches, however, the ability to precisely target the ROI remains challenging and requires endogenous landmarks (Karreman et al., 2016). To illustrate the advantages of an AT-based solution in targeting the ROI, we imaged the *Drosophila* ovarian chamber at stage 3. Our previous efforts with the ovarian chamber had already exposed us to the difficulties of localizing the ROI in this tissue, and had actually prompted us to develop our current AT method that enables more direct sampling and screening.

Drosophila oogenesis is often used to model cellular processes, such as cell division, cell migration and stem cell differentiation (Horne-Badovinac and Bilder, 2005; Fuller and Spradling, 2007; McLaughlin and Bratu, 2015). During development of the ovarian chambers, the exterior follicular cells, the internal nurse cells and the oocyte undergo numerous structural changes. Nurse cells, which supply the necessary nutrients and cell building material to the oocyte, do not accomplish abscission but remain interconnected through the network of ring canals (RCs). During development and cell growth, the initially small RCs expand in diameter by about tenfold (Robinson et al., 1994; Hudson and Cooley, 2010; McLean and Cooley, 2013; Hudson et al., 2015). Imaging the RCs in their entirety using EM is difficult, mainly because of their large size and random distribution inside the ovarian chamber. On single sections, the RCs frequently appear as two spaced bars or brackets, and not as a circular structure, as in FLM micrographs. Based on our experience, localizing the RCs with FIB-SEM or SBFSEM tomography is problematic (Loyer et al., 2015).

Development (2018) 145, dev160879. doi:10.1242/dev.160879

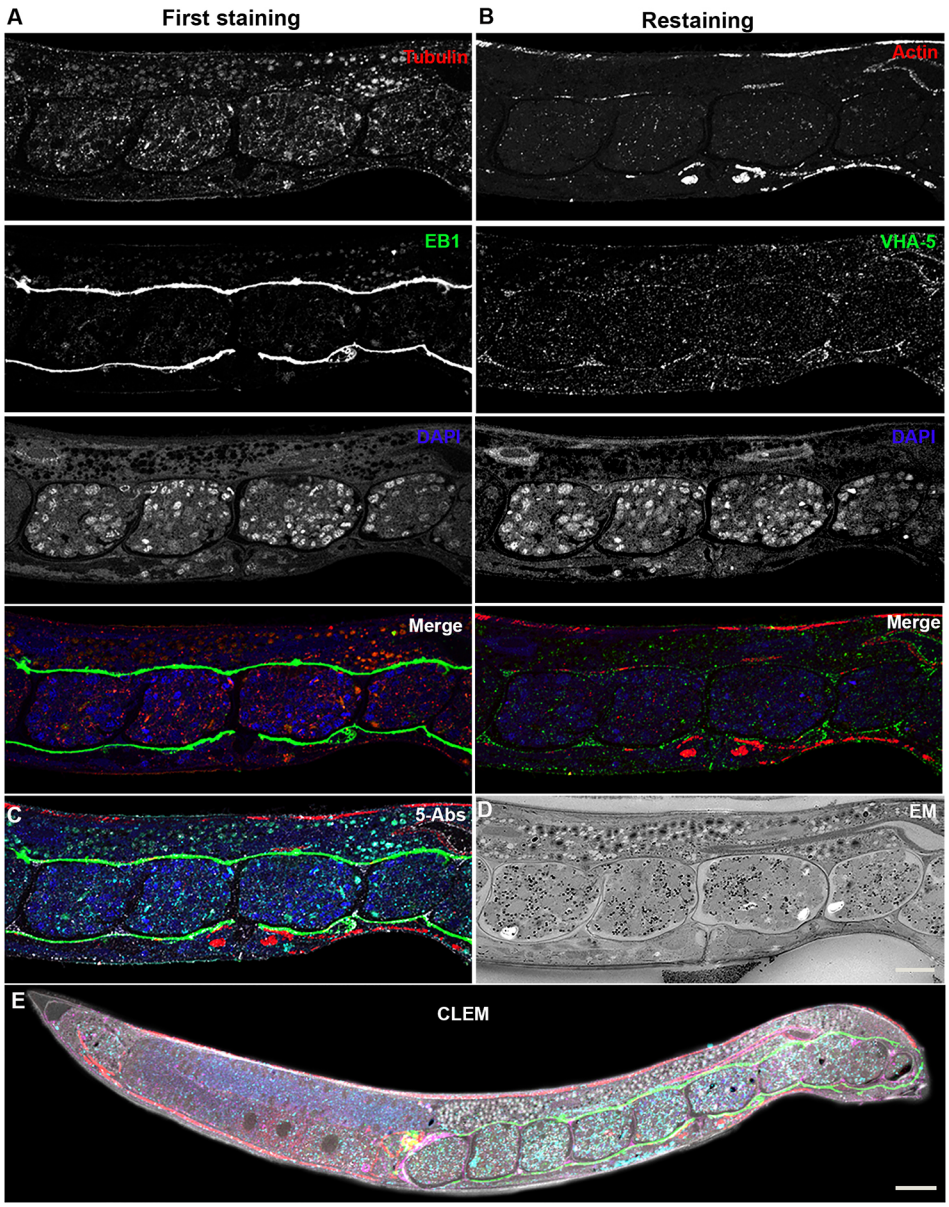

Fig. 2. Light microscopy and multiplex imaging: immunolabeled *C. elegans* sections on coverslips. (A) Merge of 25 fluorescently labeled longitudinal sections through the middle portion of a *C. elegans* adult (tubulin, red; EB1, green; DAPI, blue), and overlap of all three channels (merge). (B) Immunolabeling on the same sections after eluting the initial labeling, washing, and re-labeling with a second set of markers (actin, red; VHA-5, green; DAPI, blue). DAPI nuclear staining served as an alignment reference to combine the first and second datasets. (C) Merged image of both labeling rounds, showing all five markers (tubulin, red; EB1, green; actin, red; VHA-5, green; DAPI, blue). (D) An inverted contrast SEM image of one section from the middle of the array that corresponds to the labeled region (vulva and embryos). (E) Superposition of the quintuple immunolabeling and the EM image over the entire zone of sectioning (Movie 2). Scale bars: 10 µm.

We prepared the ovarian chambers using chemical fixation and flat embedding, sectioned them, and then transferred the ribbons of sections to wafers. Our fast screening strategy rapidly localized the RCs within the arrays of sections at low magnification. Then, we assessed the general orientation of the organism in a flat-embedded sample based on the anatomy of the sample (Fig. 3A). After sectioning, we localized the RCs based on known landmarks in the organism. For this, screening the sections on wafer at low magnification resulted in the rapid identification of regions to analyze at higher resolution (Fig. 3B,C). Initially, we collected ribbons of consecutive sections, aligned them side by side (Fig. 3B; each ribbon of sections is colored distinctly), and then tracked cellular features (or landmarks) along these ribbons. For faster screening, the sections were not screened in consecutive order but, rather, 'horizontally', by scanning the middle section from each ribbon for RCs (Fig. 3C; the color of the frame corresponds to the color of a given portion of the array, selected in proximity to the white arrow at the panel B). Once an RC was recognized and located (Fig. 3C, orange), we could easily track the entire relevant sequence of sections by sequentially following the sections along the ribbon, using the reference section as an anchor. This simplifies the screening logic: one starts from the beginning of the relevant sample portion and then collects sections for as long as necessary. In this way, the localization of anatomical features is more efficient, rapid and precise, avoiding the acquisition of unnecessary data sets.

To localize the four RCs, which connect the future ovary and the nurse cells, we applied the screening strategy described above. At low magnification, we identified RCs in sections and, as expected, the canals appeared only partially and did not resemble rings (Fig. 3D). After acquisition, the overlay of the sections allowed the modeling of the rings in their entirety, and the identification of the position of the ring on the cell surface (Movie 3). The same set of sections can be reused to reconstruct the interaction between additional pairs of cells in the same ovariole, or the sections can be re-imaged to analyze the structure of the RC in ovarioles of another developmental stage. Because the sections remain intact on the surface of the wafer, a ring of particular interest can be revisited using different acquisition parameters for more detailed study (Fig. 3E, Movie 4). The aligned data set can be further analyzed using different modeling and rendering programs, providing the

Development (2018) 145, dev160879. doi:10.1242/dev.160879

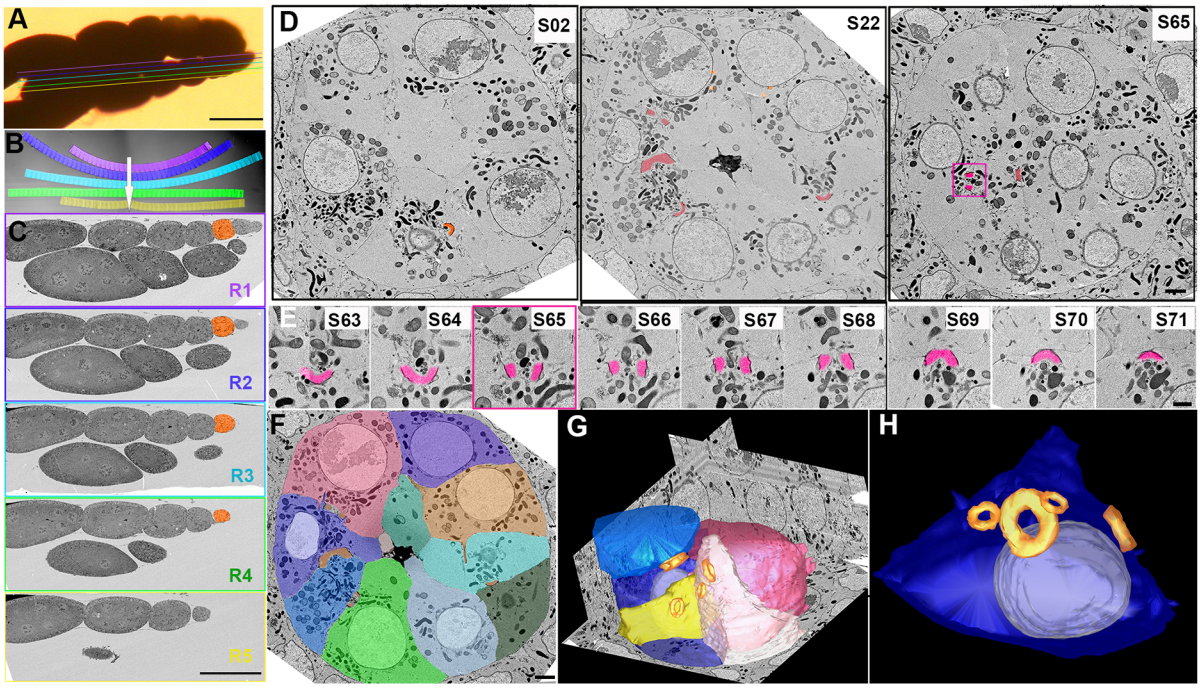

Fig. 3. Blind screening approach for morphological analysis and 3D reconstruction of AT data. (A) Image of *Drosophila* ovarioles flat-embedded in epon resin and arranged for sectioning. Line colors indicate the approximate levels of sections shown in B,C. (B) Sections collected on wafer support. Each row is color coded to correspond to the colored lines in A. (C) SEM image of 'lateral low magnification screening' strategy. Horizontally 'leaping' from one ribbon of consecutive sections to another helps to rapidly reveal the ROI in the sample, based on previous knowledge of anatomy. In this case, the ROI is the stage 3 ovarian chamber (orange), and the sections in ribbons 4 and 5 do not merit further study. (D) Selected images of low-magnification screening aimed at localizing the ROI (RCs; magenta). RCs are randomly scattered inside the ovarian sphere in random orientations and have distinct morphological characteristics. Locating ring canals by analyzing serial sections is tedious and often not successful. In contrast, rapid screening successfully facilitates this task. The magenta box indicates the canal analyzed in more detail. (Movie 3). (E) High-magnification SEM analysis of a single ROI, (an RC, pseudo colored in magenta). S65 is a high-magnification reoriented image of the boxed section in D (Movie 4). (F) A selected SEM image from the image sequence colored using the IMOD program (Movie 5). (G) Volume reconstruction of sections from the image stack. Individual cells are shown in different colours; RCs, orange. (H) A subset of the rendering dataset. Future oocyte interconnected with the nurse cells through four RCs (cell contour, dark blue; nucleus, pale blue; RCs, orange). R, ribbon; S, section. Scale bars: 100 µm in A,C; 1 mm in B; 2 µm in D; 1 µm in E.

precise identity of different cells, their spatial distribution and their interactions (Fig. 3F,G, Movie 5). The resulting data can be further mined by targeted analysis of relevant 3D data portions (Fig. 3H, Movie 5). Once the various stages of ovarian chambers and RC maturation have been collected and maintained on wafers, a library can be established. As in the case of ovarian chambers, any sample collected on wafers can be re-analyzed and re-imaged when new questions arise. Arrays can be stored indefinitely and, with proper annotation, can be used by several different research groups. In addition to the examples presented here, this strategy can be applied to answer similar questions in other complex tissues (Fig. S1).

Correlative labeling of samples on wafers: fluorescence retention

We next extended our multiplex immunolabeling protocol and 3D screening with a reconstruction strategy, focusing on an organism bearing genetically encoded fluorescent markers. To retain the endogenous fluorescence *en bloc* for AT, we tested several preparation protocols. HPF-FS in acetone-containing uranyl acetate with subsequent embedding in HM20 methacrylate resin gave the most satisfactory results. With this, we could visualize various fluorescent constructs, both *en bloc* and on section (Fig. 4A-D), facilitating the localization of the ROIs in 3D. Moreover, searching for the fluorescence signal in a light microscope helped to localize the ROI faster than using EM screening for desired morphological features. We processed *C. elegans* larvae using this protocol. In addition to the endogenous signal, the sections could be labeled with antibodies, providing additional data (Fig. 4C). Here again, the superposition of the fluorescence and the EM images was reliable and straightforward, making the direct CLEM reconstruction and analysis precise and unambiguous (Fig. 4D).

To further facilitate rapid correlation of ROIs and automate the acquisition process, we used the MAPS software (FEI). This provided automatic acquisition of both fluorescence and SEM images. We then superimposed these images, allowing the transfer of the same 'geographical' parameters from one type of microscope to another (Loussert Fonta and Humbel, 2015). Using the CorrSight light microscope (FEI) and MAPS software, large regions can be acquired automatically at low magnification (×10), with the separate single images stitched together to form one large file. This provides an overview of the sections on the support, which is useful to identify the current location within the ribbons of consecutive sections. Imaging is then carried out using various objectives, imaging modes and several fluorescence channels to localize the proteins of interest. For correlation, high-magnification (×63, ×100) large-scale images of the fluorescent structures on the relevant sections can be acquired by tiling (Fig. 5A). After light microscopy, the project, containing the recorded light micrographs, can be transferred to a scanning electron microscope (Fig. 5B). Using anatomical landmarks, all light micrographs can be aligned and overlaid on the map of the electron micrograph and high-resolution electron micrographs can be recorded (Schwarz and Humbel, 2014).

Development (2018) 145, dev160879. doi:10.1242/dev.160879

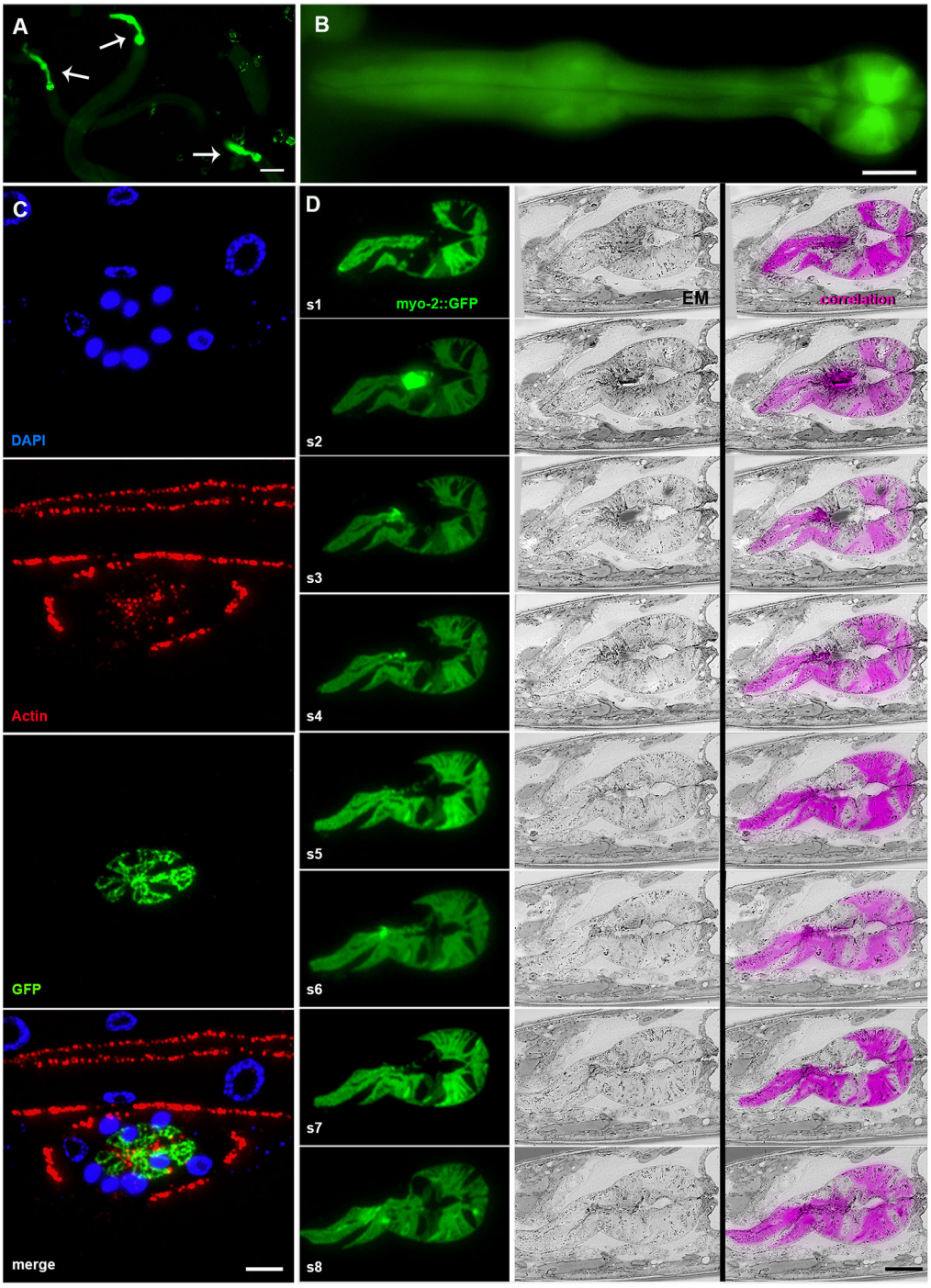

Fig. 4. *In vivo* fluorescence retention for CLEM. (A) Fluorescence image of *C. elegans* larvae embedded in resin, with *myo-2::GFP* fluorescence signal in the pharynx (arrows indicate individual larvae). (B) Fluorescence image of the *C. elegans* pharynx labeled with *myo-2::GFP*, embedded in hydrophilic HM20 resin. (C) Immunolabeling of sections through the transversely sectioned pharyngeal region of a *C. elegans* larva. The retained GFP signal (green) and additional labeling (actin for muscles, red; nuclei stained with DAPI, blue) can be seen, with 25 sections aligned and merged. (D) 3D-correlated panel of eight consecutive longitudinal sections through the pharyngeal region of a *C. elegans* larva: *myo-2::GFP* (green), inverted SEM (gray) and the merge of both types of images (GFP signal inverted to magenta for better visualization). s, section. Scale bars: 10 µm.

To highlight the versatility of this technique, we analyzed the excretory canal of *C. elegans*. This single cell organ is located in the pharyngeal region of the worm and, during development, sprouts four tubular extensions that run the length of the entire body of the animal (Fig. 5C; Kolotuev et al., 2010, 2013; Sundaram and Buechner, 2016). Fast HPF-FS preparation enabled the preservation of the fluorescence *vha-1::GFP* signal (Fig. 5D). This greatly facilitated the recognition of the ROI after transfer to SEM, as the image has a similar appearance in both modalities.

The MAPs program can facilitate the automatic acquisition of both fluorescence and SEM images, subsequently superimpose these images, and provide a result analogous to that of the 'Google Earth' principle. First, images are acquired using low magnification (Fig. 5B) and then higher magnification is used (Fig. 5E,F). Then, 'stitched images' are composed of several single images at a given resolution so that both the overall field of view and the individual images of particular ROIs can be reused for future analysis. Compared with analyzing sections on TEM grids, using arrays permits the analysis of larger sections. Thus, more individual samples can be simultaneously collected (Fig. 5E, yellow; $n>30$). The fluorescence signal is easily detected on sections, facilitating identification of animals in the desired orientation and/or developmental stage. After the sample is identified with FLM, SEM data can be acquired either by manually correlating the position of the sections, or by using a MAPS-mediated site localization. After the ROI has been found on a reference section,

Development (2018) 145, dev160879. doi:10.1242/dev.160879

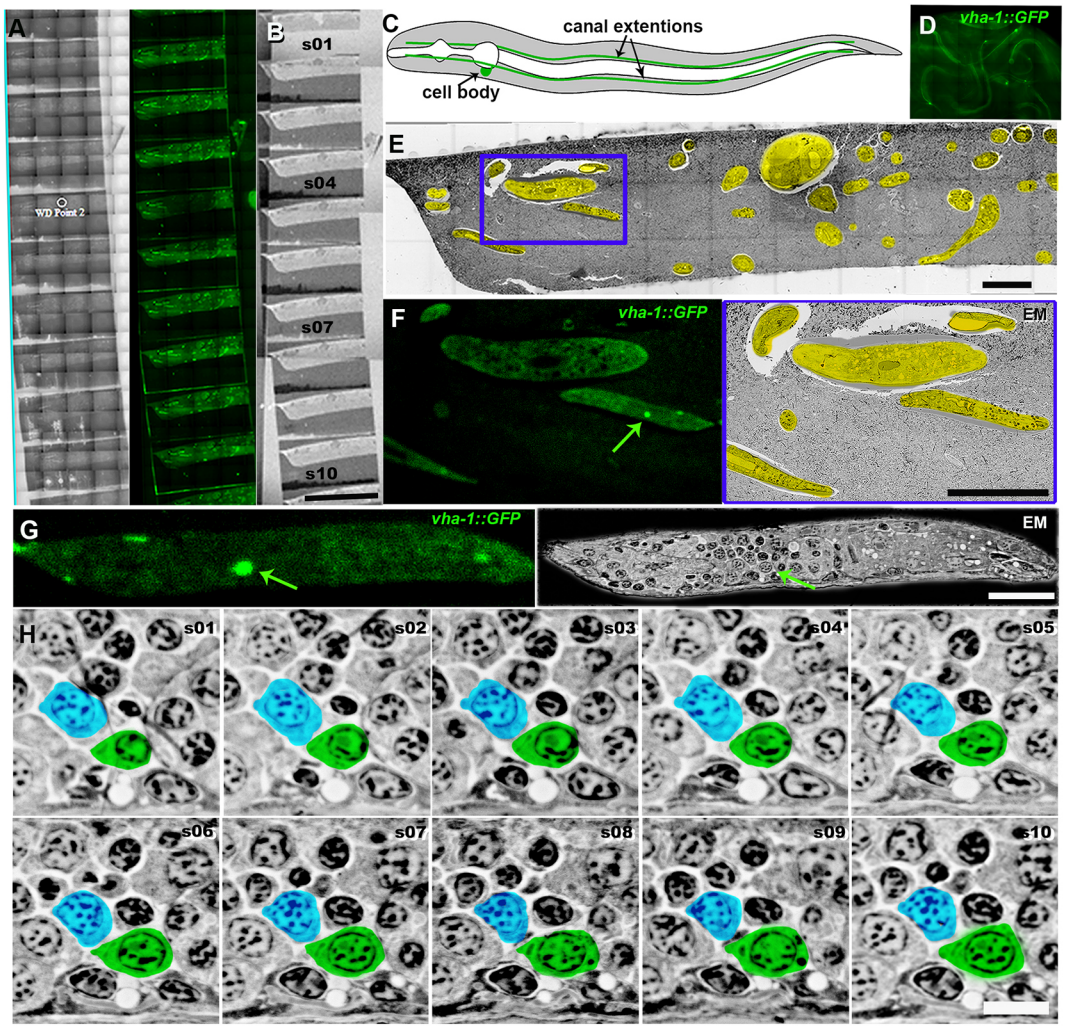

Fig. 5. MAPS-mediated screening strategy: *C. elegans* excretory canal. (A) An array of sections on a wafer visualized by the light microscopy reflection mode and GFP signal visualized by CorrSight MAPs-based tiles acquisition. (B) The same array visualized with the BSE-SEM. (C) A schematic of the *C. elegans* excretory canal (green) with the cell body and four lateral tubular extensions. (D) *C. elegans vha-1::GFP* larvae embedded in hydrophilic HM20 resin after HPF-FS. Excretory canal fluorescence is preserved. (E) An EM image of a representative section on a wafer acquired with BSE-SEM detector at low magnification. Numerous *C. elegans* samples present in this section are highlighted in yellow. This overview of the content of the section can help during pre-screening of multiple sections before starting the EM part of CLEM analysis. The blue box designates the portion of the image represented in F. (F) Enlarged view of the boxed area in E. GFP image of *vha-1::GFP* labeling of the excretory canal on the section and the same area visualized with BSE-SEM (green arrow highlights the excretory canal cell body). (G) A side-by-side fluorescence and EM image of the sample shown in F (reoriented). Arrow indicates the excretory cell body. (H) A sequence of inverted SEM images of the excretory canal cell from the subsequent sections. Excretory cell, green; random neighbor cell, blue. Note that the cells surrounding the labeled cells appear identical, and in the absence of the superposition, it might be difficult to recognize the cell of interest. s, section. Scale bars: 500 nm in A,B; 50 µm in E; 10 µm in F, G; 5 µm in H.

one can select the desired resolution for the EM acquisition (Fig. 5G,H). Then the necessary ultrastructural data can be obtained by volume reconstruction. Within the tissue, the desired cell type can be ultrastructurally indistinguishable and/or difficult to localize. One example is the cell body of the early larval stage excretory canal, which is located in a densely packed environment and is not evident on routine ultra-thin sections. The fluorescence signal can aid in identifying a particular cell at the ultrastructural level (Fig. 5G). Once the fluorescence signal allows recognition of the cell of interest, EM analysis of the subsequent sections no longer requires correlation with the fluorescence data: the position of the cell on subsequent sections becomes evident (Fig. 5H).

The adult excretory canal extension is 100-1000 µm long and 50-100 nm in diameter, making it difficult to image the overall volume of the canal arms using SEM. Only very rarely does the fixed animal remain straight after processing, so orienting for longitudinal sectioning is a tedious procedure. Usually, only a small portion of the body can be correctly oriented. Locating an ROI may require screening and acquisition of hundreds of carefully collected serial sections (Fig. 6A). Thus, it is complicated to orient precisely these extensions for longitudinal sectioning. The specimen often curves after fixation, and the recognition of the defragmented structure without the overall body context is often difficult, as the same structure appears different, and in a different location, depending on the sectioning axis (Fig. 6B). In this case, the fluorescence serves as a landmark to permit the easy recognition of the cells of interest. For this purpose, we labeled the excretory cell in green and a random cell in its vicinity in blue. Superficially, these cells appeared identical, and if one had to distinguish them by a 'blind search', it might be impossible.

Here again, the combination of fluorescence-mediated screening with subsequent targeted EM acquisition facilitates precise orientation.

Development (2018) 145, dev160879. doi:10.1242/dev.160879

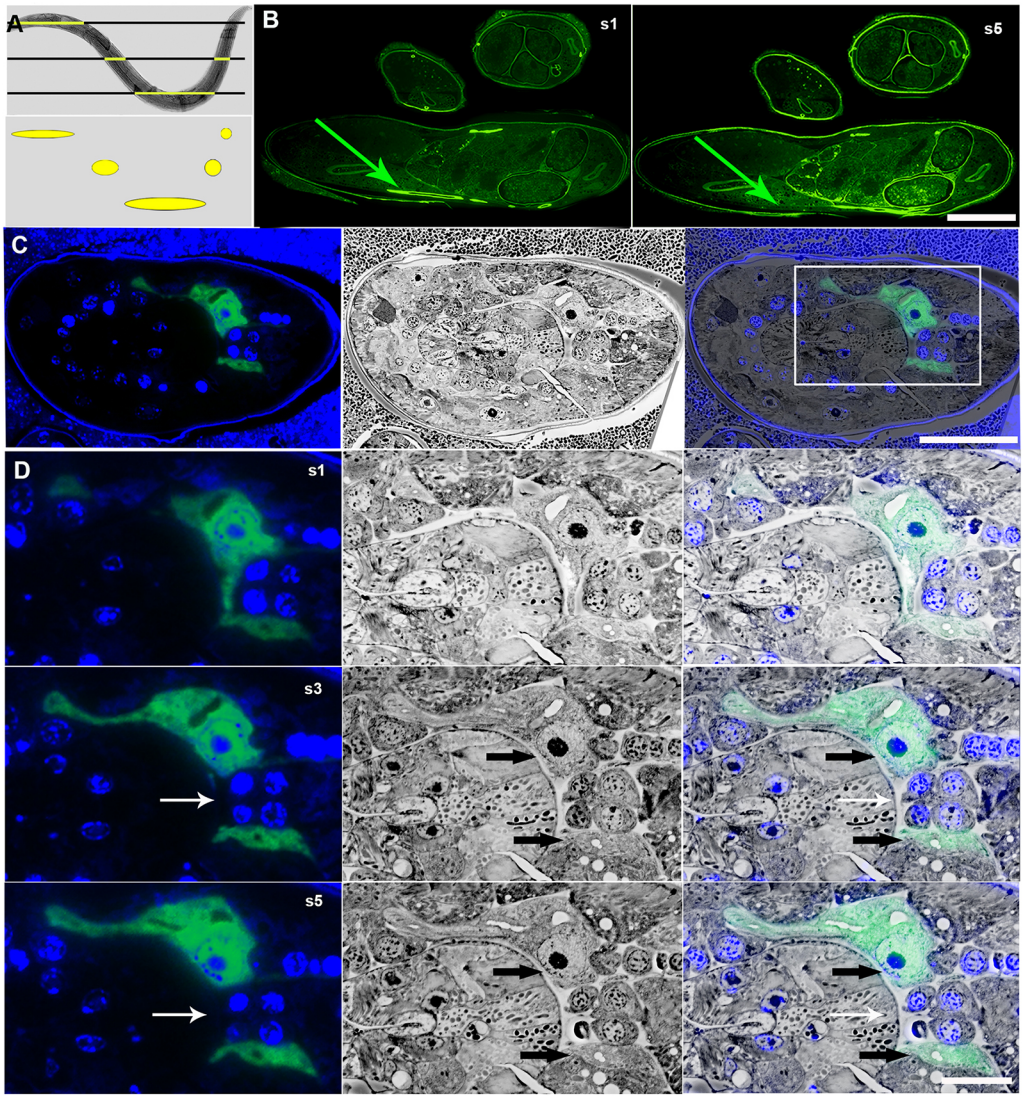

Fig. 6. AT of nonlinear sample. (A) A *C. elegans* larva embedded in hydrophilic HM20 resin to illustrate the result of ultra-thin sectioning. Diagram shows the outcome of the sectioning. Note that on the section, the same animal might appear as two independent samples if it is sectioned in the upper part. (B) Fluorescence images of two random fluorescent sections spaced by 500 nm of the excretory canal GFP signal on sections one and five. (C) An oblique section of a *C. elegans* larva at the level of excretory canal cell body: *vha-1::GFP*, BSE-SEM and merged images. The white box indicates the position of D. (D) Representative sections of the excretory canal cell body of a *C. elegans* larva and its lateral extensions. White arrow indicates the disappearing part of the canal. On the EM micrographs without the fluorescence, it might be difficult to recognize that two parts belong to the same structure (black arrows). s, section. Scale bar: 50 µm in B; 10 µm in C; 2 µm in D.

First, the appropriate fluorescence image is found on section. It is useful to label the sections with a nuclear marker (e.g. DAPI, Draq5) to assess the orientation of the sample and to avoid confusion in repositioning the fluorescence signal on the EM data. Second, fluorescence data rapidly guides the analysis to the relevant ROI, after which the required number of sections or the desired volume of data is collected (Fig. 6C). In our example, the sections are spaced less than 200 nm apart, and the portion of the canal that connects the extension to the cell body is no longer seen from one section to another (Fig. 6D, arrow). Without fluorescence, the detached part would not have been evident using EM data only (Fig. 6, arrows).

Our results demonstrate that when the endogenous fluorescence signal is preserved throughout the preparation, the random-sectioning approach facilitates identification of randomly oriented samples. When combined with the MAPS correlation software, the structures of interest can be rapidly identified and imaged at high resolution by EM, enabling fast-throughput analysis of a statistically significant number of organisms.

DISCUSSION

This study presents an efficient AT procedure to facilitate the analysis of a single ROI in a whole organism on serial sections that is applicable for numerous biological samples. On serial sections, the ROI can be labeled with a fluorescent tag and correlated with the corresponding electron micrograph. The serial sections can then be quickly screened using fluorescence labeling or directly using SEM.

Besides the SEM, our method does not require additional expensive equipment for an EM lab or facility. The newly designed diamond knife we introduce can be used with any ultramicrotome, and its application is technically easier than performing classical ultra-thin sectioning. In contrast, the approach using SBFSEM with FIB-SEM has a very high cost and limited accessibility. An alternative approach using the ATUMtome machine for automatic section collection from neuronal samples was recently demonstrated (Kasthuri et al., 2015). Likewise, an alternative AutoCUTS method was recently used to collect sections of *C. elegans* larvae (Li et al., 2017). However, this time-consuming and more expensive strategy is only worthwhile when there is a requirement for thousands of sections, as is often needed for brain samples. In contrast, our direct AT method requires a modified diamond knife, whereas the ATUMtome strategy requires an expensive and specialized machine (available at selected facilities only).

For both the ATUMtome and our direct AT method, libraries of serial sections can be stored indefinitely and re-analyzed to address future research questions. For studies involving multiple organisms or organs, for which neither serial section TEM nor volume EM

Development (2018) 145, dev160879. doi:10.1242/dev.160879

approaches would be efficient, our screening method provides an accessible solution. For questions that can best be answered by analyzing many different samples (e.g. wild type versus mutants), libraries of AT sections can be extremely useful. A single 2×4 cm wafer can contain all the necessary information to permit the analysis of a small organism quickly. Also, the researcher need not immediately acquire the entire sectional area at high resolution, as is required for block-face microscopy. High-resolution collection of only the relevant data results in greater precision and shorter acquisition time. Fewer electronic data are stored, as information that is irrelevant to the initial question is not collected. Thus, statistically significant EM volume data can be acquired in a timely fashion. Further, compared with block-face methods, the sections generated by AT can first be imaged at low magnification for orientation, and then the ROI can be imaged at higher resolution for a more detailed analysis. Direct CLEM, with or without automation, can provide an additional level of volume correlation and can simplify the EM identification of similar structures. The fields of cell and developmental biology, model organism analysis, and even clinical research could benefit from this technique, to address such mechanisms as cell migration, tissue remodeling, and the fine structure of cell division and abscission (Fig. S1).

Most of the technical problems with the use of the existing SEM imaging fields and modalities relate to the lack of precision of automatic acquisition. Current software systems that support AT include Atlas, with Zeiss scanning electron microscopes, and MAPS, with FEI electron microscopes. With both software systems still in development, future improvements could facilitate the automation of robust and efficient serial section acquisition; for example, the acquisition process could be automated, and more solid and user-friendly data alignment algorithms could be provided.

In conclusion, our AT method can be used to resolve long-standing questions in cell and tissue biology that require 3D ultrastructural analysis, and to localize antigens in defined structures. This approach could be useful for both biological research and clinical analysis, as high-quality results can be efficiently achieved using equipment that is, to a large extent, already present in many imaging facilities.

MATERIALS AND METHODS

Sample fixation and processing

The samples were either chemically fixed or processed using the HPF-FS method (Table 1).

Chemical fixation

The samples were fixed for 2 h at ambient temperature in 2% (w/v) formaldehyde and 2.5% (w/v) glutaraldehyde dissolved in 0.1 M phosphate buffer, pH 7.4 (EMS, 19340-72, 11650, 19344-10, respectively). They were then post-fixed in 1% (w/v) osmium tetroxide (EMS, 19152) and 1.5% (w/v) potassium ferricyanide in cacodylate buffer (EMS, 26604 1A) for 1 h at ambient temperature, followed by 1 h incubation in 1% (w/v) tannic acid (Sigma-Aldrich, 403040). After extensive washes in water, the samples were incubated in 2% osmium tetroxide followed by 1 h in 1% (w/v) uranyl acetate in water and dehydrated in an ascending series of ethanol followed by an ascending concentration of Epon (EMS, 1420) in ethanol mixtures (Starborg et al., 2013; Kolotuev, 2014). Finally, the samples were flat embedded using a two-step procedure, and then polymerized at 60°C for 48 h as previously described (Fig. 1A, Table 1; Kolotuev, 2014).

Cryofixation quick freeze-substitution

HPF-FS was performed using a modified version of the previously described method (McDonald, 2014). Carriers containing HPF-immobilized samples were transferred to vials containing freeze substitution media [0.1% (w/v) uranyl acetate, 2% (v/v) H_2O in acetone] and then placed in the freeze-substitution unit (AFS2, Leica Microsystems), cooled to −140°C, and heated to −50°C over 8 h. The samples were then infiltrated by ethanol and resin mixtures. After freeze-substitution, the samples were flat embedded, either in Epon embed 812 resin (EMS, 1420 morphology analysis), or in the monostep HM20 hydrophobic methacrylate resin (EMS, 14340) for the samples containing fluorescently tagged proteins, or those to be used for immunofluorescent labeling (Table 1; Kolotuev, 2014).

Block preparation and serial sectioning

Blocks were trimmed to ∼100×200 µm cuboids using a trim 90-diamond blade (Diatome). Sample block sides parallel to the knife were coated with a mixture of one part Weldwood contact cement (Néoprène Liquide, Sader) to three parts xylene. This mixture increased the adhesiveness of the sections to each other to produce a long ribbon of consecutive sections (>300). The resulting long ribbons of consecutive sections were subdivided into shorter ribbons (50-100 sections) and then aligned on support, side by side (Kolotuev, 2014).

To generate planar arrays of sections on support, we used a modified ultra 35° diamond knife with a custom-built boat (Fig. 1C,D; Diatome; see Results for details) mounted on a UC7 ultramicrotome (Fig. 1E; Leica Microsystems). Ribbons of consecutive sections were generated with a length that varied according to the eventual goal of the AT procedure: 50-200 sections per ribbon, 50-150 nm thick. Each array of ribbons aimed for multi-labeling was transferred to a glass coverslip (VWR, 631-1575), or, if it was dedicated for EM reconstructions and CLEM, to a silicon wafer (Ted Pella, 16015). Before use, glass coverslips were cleaned and coated with 0.5% gelatin solution (EMS, 16564) added to 0.05% chromium potassium sulfate (Sigma-Aldrich, 243361), following a previously described procedure (Micheva et al., 2010). We followed the manufacturer's instructions to obtain a 1-2 nm carbon layer for the samples collected on the glass slide using CCU-0101 LV machine (Safematic). A thicker layer can compromise the quality of the SEM images. Image collection on the ITO-coated slides should eliminate the need in this step (I.K. and A.M., unpublished observation,).

Round wafers were cut into 2×4 cm rectangles using glass breaking pliers 6″ (Ted Pella, 7295), cleaned, and glow discharged for 30 s using the current plasma HT of 15 mA (Cressington 208, Cressington Scientific Instruments). We did not carbon coat the samples on wafers because we did not detect any charging effect during the image acquisition.

Improving quality of arrays on sections: avoiding folds

Sectioning problems can compromise both the quality of the sample and the reliability of the subsequent analysis. The appearance of wrinkles on the surface of sections can ruin the entire AT data set. The impact of a fold on data analysis is difficult to quantify, mainly because only folds that affect the ROI are deleterious.

We distinguished two types of wrinkles that can appear on the surface of sections: (1) folds, causing global damage to the section, and (2) microfolds, small wrinkles in limited areas of the sample surface. We could detect both types of wrinkles on sections, but frequently they affected only the excess embedding resin surrounding the sample. Also, on several sections, the wrinkles could be found on the sample surface, without affecting the ROI (Fig. S2). Even in very extreme cases of severe wrinkles, it is difficult to interpret their impact on data analysis. In Fig. S3, four independent samples of a section are shown. Even if samples 1, 2, or 3 have large folds or debris, this will not affect the data analysis. However, if sample 4 had a fold in the bottom half, it would only be ruined if we were interested in its bottom half. If we wanted to analyze its upper half, then the wrinkle would not affect our analysis. The situation with microfolds is very similar if they happen to occur within the sample but not within the ROI (Fig. S3). Thus, we decided not to quantify the number of folds but, rather, to characterize the conditions under which they appear and possible ways to prevent them.

Below we list factors that can lead to folds and wrinkles and how these can be minimized.

Block surface size and section homogeneity

The size of the sample surface appears to be essential: smaller sections result in fewer wrinkles because there is less surface to generate wrinkles. Further, density differences within the sample can influence the quality of

Development (2018) 145, dev160879. doi:10.1242/dev.160879

sectioning. Epoxy resin will create a copolymer within the biological sample, which has a different density than the empty resin. Thus, excess embedding resin should be removed. Within homogeneous tissue, all excess resin is removed, leaving only a rectangular block of embedded tissue. For smaller non-homogeneous samples, such as *C. elegans* or *Drosophila*, it is difficult or impossible to remove the entire resin around the sample. Thus, we advise maintaining a similar amount of resin on each side of the sample.

For better stability of the ribbon of consecutive sections, it is important to trim the block as close to the sample as possible, shaping its surface into a rectangle, with the edge touching the knife measuring twice the width of the edges at the side. A larger section surface produces more folds, whereas sections with a smaller surface tend to curve more. Curving of the ribbon of consecutive sections (section curling) is problematic, especially for ribbons that will be aligned side by side on support. With some experience, this problem can be overcome (Movie 1).

Section thickness

This parameter is as important as the block edge size and has a significant effect on the quality of the resulting sections. Ultra-thin (50-80 nm) sections attach better to the support and have fewer microfolds compared with semi-thin sections (100-250 nm).

The speed of water retraction during section drying

We found the rate of water retraction to be crucial for successful transfer of the ribbons of consecutive sections to the slide support. The support surface should be hydrophilic. Excessive hydrophobicity of the support can cause folds in the sections. Thus, supports dedicated for SEM analysis (wafers, glass slides or Kapton tape) should be carefully pretreated using a standard glow discharge procedure. Even with a very disorganized collection of sections, if the process of drying is optimal, there is a lower chance of the appearance of folds (Fig. S4, can be zoomed in) and the development of microfolds in non-homogeneous samples is much less likely to occur.

Occasional debris on the section surface can be difficult to eliminate. To reduce the occurrence of debris, the knife and the basin must be meticulously rinsed with distilled water filtered with a 0.22 µm syringe filter. Coated glass slides must be carefully prepared, and wafers thoroughly cleaned. Water filtering and knife cleaning before the generation of the sections can help to minimize the accumulation of dust and debris on the surface of the sections.

Sample treatment for FLM, EM, and CLEM

For multiplex fluorescent labeling, the arrays were labeled with a subset of different antibodies using a previously described procedure (Micheva et al., 2010). Briefly, ribbons of consecutive sections on a glass coverslip were incubated in a humidity chamber with 50 mM glycine solution in TBS (Sigma-Aldrich, T5030) for 5 min, then with blocking solution containing 0.1% BSAc (Aurion, 900-099) in TBS for 5 min. Specific primary antibodies mouse anti-actin (Cedarlane, CLT 9001), mouse anti-tubulin (Invitrogen, 322500), rabbit anti-VHA5 (courtesy of Dr Labouesse, Institut de Biologie, Paris, France) and rabbit anti-EB1 (Santa Cruz, SC 15347) were diluted to 1:100 v/v in TBS and incubated overnight at 4°C (Nicolle et al., 2015). Secondary antibodies Cy2 anti-mouse (Abcam, Ab-6944) and Cy3 anti-rabbit (Abcam, Ab-6939) were diluted to 1:100 v/v in TBS and incubated at ambient temperature for 2 h.

Samples were mounted using the Vectashield Antifade Mounting Medium (Vector Laboratories, H1200) and imaged the same day. Destaining and relabeling of the arrays was performed according to the experimental requirements (Micheva and Smith, 2007). For removing the bound antibody complex, a mixture of 0.2 M NaOH with 0.02% SDS was applied to the samples for 20 min, followed by extensive washing cycles. Before relabeling using the same method as the initial labeling, the samples were dried in an oven at 60°C for 20 min.

After completion of fluorescence image acquisition, the samples were extensively washed in double-distilled water, dried and contrasted for 15 min in a 4% uranyl acetate solution followed by a 10 min incubation in Reynolds' lead citrate solution.

For SEM acquisition, samples prepared using the high-contrast procedure were directly observed without further manipulation. For all other acquisitions, the sample contrast was increased using the same parameters as for CLEM experiments.

Fluorescence on sections

Multiple fluorophores and fluorescence preservation procedures for CLEM have been developed (Nixon et al., 2009; Kukulski et al., 2011; Watanabe et al., 2011; Peddie et al., 2014; McDonald, 2014; Burette et al., 2015; Johnson et al., 2015; Kopek et al., 2017). Although efficient for many types of proteins, the level of fluorescence of genetically encoded markers on sections varies from construct to construct. Although we did our best, we could not predict under which preparation conditions it would be preserved at all, and to what extent. For some constructs, fluorescence remains visible inside the block and on sections even without using an anti-bleaching solution. For other samples, even if we were not able to detect a signal inside the block the fluorescence was often visible in the sections. For these samples, we could preserve the fluorescence signal for at least 1 year after the preparation. For some samples, however, although the fluorescence signal was initially present, we were not able to preserve the fluorescence in blocks or on section. A systematic analysis of fluorescence preservation as a function of a protein type (transmembrane, cytosolic, secretory, etc.) could further facilitate our understanding of the problem of fluorescence preservation. In the future, we hope to combine our observations with those of other groups that have experience with fluorescence retention using other species and fluorescent constructs to understand the factors influencing fluorescence retention and to develop a robust preparation protocol.

Intuitively, thicker sections should provide a better fluorescence signal when genetically encoded markers are used. However, there is a thickness-to-stickiness relation, in addition to the loss of EM details in thicker sections: thinner sections had better adherence to the surface. Also, photobleaching was even more of a problem. Thus, to find a reliable way to quantify the 'signal emission' from sections of different thickness might require complicated math/physics calculations, which would likely not be applicable for all types of fluorescent constructs. However, the overall preservation of sectional fluorescence is a concern because, after fixation, the signal is not linear and varies with the type of construct.

Image acquisition

Fluorescent microscopy acquisition and image treatment

Wide-field fluorescence image acquisition was made using a Leica DMIRB inverted microscope or a Leica DMRXA upright microscope equipped with a 20×/0.4 NA plan, a 63×/0.7 NA PL Fluotar or 100×/0.7 air and 1.4 NA PL APO oil objectives, and a Coolsnap HQ2 CCD camera (Photometrics).

Confocal fluorescence images were taken using a TCS SP8-SMD confocal microscope equipped with both 63×/1.4 NA Oil HC PL APO and 40×/1.3 NA Oil HC PL APO objectives (Leica Microsystems). Fluorescence signals were collected sequentially through photon-counting hybrid detectors (Leica) to increase the signal-to-noise ratio.

Light microscopy

For light microscopy tile acquisitions, the CorrSight light microscope running the MAPS software was used (Loussert Fonta and Humbel, 2015). The microscope was equipped with Zeiss objectives: 5× NA 0.15, 20× NA 0.8, 40× NA 0.9 and 40× NA 1.3 oil immersion; and DAPI, 488 nm and mCherry filters. The light micrographs, bright-field and fluorescence images were recorded with MAPS and stored as an aligned package in a project.

SEM acquisition

For SEM acquisition, we used a JEM 7800F with retractable backscattered electron detector (JEOL) with the following parameters: accelerating voltage, 8 kV; probe current, 1.6 nA; WD, 5 mm; dwell time, 10 µs/pix; frame size, 4096×4096. For MAPS-related experiments, Quanta FEG 250 SEM (FEI) was used with the following parameters: accelerating voltage, 10 kV; probe current: 0.8 nA; WD, 7 mm; dwell time, 30 µs/pix; frame size, 4096×4096. The MAPS projects were transferred to the Helios 650 FIB-SEM (ThermoFisher). A reference image was taken with SEM. Light micrographs were then aligned to this image and used to find the ROI to be analyzed at high resolution using SEM (Loussert Fonta and Humbel, 2015).

Development (2018) 145, dev160879. doi:10.1242/dev.160879

Alignment and reconstruction

To align the fluorescent stacks of sections, we developed the computational volumetric analysis protocol, based on Fiji and ICY programs (Schindelin et al., 2012; de Chaumont et al., 2012). The coregistration procedure will depend on the data set. Using Fiji software, we selected *C. elegans* embryos in each stack using an automatic threshold, and signals located outside of the chosen area were deleted. The first two steps can be done automatically using a rigid registration. Indeed, as images come from the same array with a microscope always using the same settings, the displacements between two images are rotation and translation. In the image processing community, numerous algorithms aim to solve the rigid registration task. We used the 'Register Virtual Stack Slices' feature available on Fiji (imagej.net/Register_Virtual_Stack_Slices). This method uses the SIFT feature to find corresponding regions in image pairs. To facilitate the use of this registration algorithm for array data, we developed a Fiji macro that runs in three steps. (1) 'Split Stack': this step splits the array hyperstack into various image sequences, one sequence for each staining of the FLM data. The sequences are stored in output subfolders. The operator need only specify the number of channels (i.e. staining) in the stack. (2) 'Register Reference': this step calculates the registration transformation matrices using the reference staining. Usually, the DAPI staining is used as a reference for FLM. The operator needs only to provide the reference channel directory, and the output directory where the transformation matrices will be stored. This directory is already created by the macro, the operator can simply select it. The algorithm settings are: Reference channel, channel used to estimate the transformation; Registered image size, size of the output image canvas. It should be larger than the original image for all of the images that have been transformed to fit into the canvas. (3) 'Apply transformation': this step applies the transformations calculated in (2), to all of the staining series.

The co-registration procedure will depend on the data set. Depending on the image content, the registration algorithm may fail to locate any corresponding regions between the separate array images. This can be resolved using pre-filtering of the reference staining before registration (i.e. between step 1 and step 2). The operator can then apply a filter to enhance the brightness, the contrast, or the gradient of the array. This optional step had not been implemented in the macro because it is application dependent. The use of the macro is similar to registering light microscopy and EM array, but for the EM alignment, a single channel is used. For the complete macro, please see supplementary material.

EM/FLM registration cannot be done automatically because the resolution and the content of images are different. Thus, a supervised registration method is required. For this, landmarks that match the reference regions on FLM and EM micrographs are used with the ICY plugin ec-CLEM (Paul-Gilloteaux et al., 2017). We coregistered arrays obtained with the macro described above and registered the first image of the FLM array and the first image of the EM array with ec-CLEM. A detailed tutorial of ec-CLEM is available at icy.bioimageanalysis.org/plugin/ec-CLEM. ec-CLEM generates a file containing the registration transformation matrix. The operator can then apply this transformation to all of the FLM arrays with ec-CLEM.

For the SEM data alignment and 3D modeling, we used IMOD (University of Colorado), Fiji (LOCI), and Photoshop (Adobe) software (Schindelin et al., 2012; Kremer et al., 1996). To achieve a TEM-like appearance, the SEM micrographs were contrast-inverted using IMOD or Photoshop.

Acknowledgements

We thank the following colleagues for their help: Kristina Micheva, Gareth Griffiths, Lucy O'Brien, Till Matzat, Paola Moreno-Roman and Karen Lunde for critical reading of the manuscript and fruitful discussions. We thank Loic Joanny (SCANMAT, Université de Rennes 1) for help with the SEM, Jean Daraspe for sharing the 3Dmod script, Willy Blanchard for the macro imaging and Tom Garber for the help in 3D image rendering.

Competing interests

H.G. is a co-founder of Diatome, a company manufacturing diamond knives for ultramicrotomy.

Author contributions

Conceptualization: I.K.; Methodology: A.B., M.-T.L., H.G., I.K.; Software: S.P.; Validation: H.G., I.K.; Data curation: I.K.; Writing - original draft: I.K.; Writing - review & editing: I.K.; Visualization: A.B., M.-T.L., C.C., A.M., S.D., B.M.H., I.K.; Supervision: I.K.; Project administration: I.K.; Funding acquisition: B.M.H., T.G., I.K.

Funding

The project was supported by the Université de Rennes 1; the Centre National de la Recherche Scientifique; and the Institut National de la Santé et de la Recherche Médicale, under an internal 'risky projects' grant.

Supplementary information

Supplementary information available online at
http://dev.biologists.org/lookup/doi/10.1242/dev.160879.supplemental

References

Anderson, J. R., Jones, B. W., Watt, C. B., Shaw, M. V., Yang, J. H., Demill, D., Lauritzen, J. S., Lin, Y., Rapp, K. D., Mastronarde, D. et al. (2011). Exploring the retinal connectome. *Mol. Vis.* **17**, 355-379.

Blazquez-Llorca, L., Hummel, E., Zimmerman, H., Zou, C., Burgold, S., Rietdorf, J. and Herms, J. (2015). Correlation of two-photon in vivo imaging and FIB/SEM microscopy. *J. Microsc.* **259**, 129-136.

Bock, D. D., Lee, W.-C. A., Kerlin, A. M., Andermann, M. L., Hood, G., Wetzel, A. W., Yurgenson, S., Soucy, E. R., Kim, H. S. and Reid, R. C. (2011). Network anatomy and in vivo physiology of visual cortical neurons. *Nature* **471**, 177-182.

Bosch, C., Martinez, A., Masachs, N., Teixeira, C. M., Fernaud, I., Ulloa, F., Perez-Martinez, E., Lois, C., Comella, J. X., DeFelipe, J. et al. (2015). FIB/SEM technology and high-throughput 3D reconstruction of dendritic spines and synapses in GFP-labeled adult-generated neurons. *Front. Neuroanat.* **9**, 60.

Bumbarger, D. J., Crum, J., Ellisman, M. H. and Baldwin, J. G. (2007). Three-dimensional fine structural reconstruction of the nose sensory structures of Acrobeles complexus compared to Caenorhabditis elegans (Nematoda: Rhabditida). *J. Morphol.* **268**, 649-663.

Burette, A., Collman, F., Micheva, K. D., Smith, S. J. and Weinberg, R. J. (2015). Knowing a synapse when you see one. *Front. Neuroanat.* **9**, 100.

Bushby, A. J., Mariggi, G., Armer, H. E. J. and Collinson, L. M. (2012). Correlative light and volume electron microscopy: using focused ion beam scanning electron microscopy to image transient events in model organisms. *Methods Cell Biol.* **111**, 357-382.

Caplan, J., Niethammer, M., Taylor, R. M., II and Czymmek, K. J. (2011). The power of correlative microscopy: multi-modal, multi-scale, multi-dimensional. *Curr. Opin. Struct. Biol.* **21**, 686-693.

Collman, F., Buchanan, J., Phend, K. D., Micheva, K. D., Weinberg, R. J. and Smith, S. J. (2015). Mapping synapses by conjugate light-electron array tomography. *J. Neurosci.* **35**, 5792-5807.

de Chaumont, F., Dallongeville, S., Chenouard, N., Hervé, N., Pop, S., Provoost, T., Meas-Yedid, V., Pankajakshan, P., Lecomte, T., Le Montagner, Y. et al. (2012). Icy: an open bioimage informatics platform for extended reproducible research. *Nat. Methods* **9**, 690-696.

Denk, W. and Horstmann, H. (2004). Serial block-face scanning electron microscopy to reconstruct three-dimensional tissue nanostructure. *PLoS Biol.* **2**, e329.

Doroquez, D. B., Berciu, C., Anderson, J. R., Sengupta, P. and Nicastro, D. (2014). A high-resolution morphological and ultrastructural map of anterior sensory cilia and glia in *Caenorhabditis elegans*. *eLife* **3**, e01948.

Fuller, M. T. and Spradling, A. C. (2007). Male and female Drosophila germline stem cells: two versions of immortality. *Science* **316**, 402-404.

Hayworth, K. J., Morgan, J. L., Schalek, R., Berger, D. R., Hildebrand, D. G. C. and Lichtman, J. W. (2014). Imaging ATUM ultrathin section libraries with WaferMapper: a multi-scale approach to EM reconstruction of neural circuits. *Front. Neural Circuits* **8**, 68.

Heymann, J. A. W., Hayles, M., Gestmann, I., Giannuzzi, L. A., Lich, B. and Subramaniam, S. (2006). Site-specific 3D imaging of cells and tissues with a dual beam microscope. *J. Struct. Biol.* **155**, 63-73.

Horne-Badovinac, S. and Bilder, D. (2005). Mass transit: epithelial morphogenesis in the Drosophila egg chamber. *Dev. Dyn.* **232**, 559-574.

Horstmann, H., Körber, C., Sätzler, K., Aydin, D. and Kuner, T. (2012). Serial section scanning electron microscopy (S3EM) on silicon wafers for ultra-structural volume imaging of cells and tissues. *PLoS ONE* **7**, e35172.

Hudson, A. M. and Cooley, L. (2010). Drosophila Kelch functions with Cullin-3 to organize the ring canal actin cytoskeleton. *J. Cell Biol.* **188**, 29-37.

Hudson, A. M., Mannix, K. M. and Cooley, L. (2015). Actin cytoskeletal organization in drosophila germline ring canals depends on Kelch function in a Cullin-RING E3 ligase. *Genetics* **201**, 1117-1131.

Jahn, M. T., Markert, S. M., Ryu, T., Ravasi, T., Stigloher, C., Hentschel, U. and Moitinho-Silva, L. (2016). Shedding light on cell compartmentation in the candidate phylum Poribacteria by high resolution visualisation and transcriptional profiling. *Sci. Rep.* **6**, 35860.

Johnson, E., Seiradake, E., Jones, E. Y., Davis, I., Grünewald, K. and Kaufmann, R. (2015). Correlative in-resin super-resolution and electron microscopy using standard fluorescent proteins. *Sci. Rep.* **5**, 9583.

Development (2018) 145, dev160879. doi:10.1242/dev.160879

Karreman, M. A., Hyenne, V., Schwab, Y. and Goetz, J. G. (2016). Intravital correlative microscopy: imaging life at the nanoscale. *Trends Cell Biol.* **26**, 848-863.

Kasthuri, N., Hayworth, K. J., Berger, D. R., Schalek, R. L., Conchello, J. A., Knowles-Barley, S., Lee, D., Vázquez-Reina, A., Kaynig, V., Jones, T. R. et al. (2015). Saturated reconstruction of a volume of Neocortex. *Cell* **162**, 648-661.

Kizilyaprak, C., Daraspe, J. and Humbel, B. M. (2014). Focused ion beam scanning electron microscopy in biology. *J. Microsc.* **254**, 109-114.

Knott, G., Rosset, S. and Cantoni, M. (2011). Focussed ion beam milling and scanning electron microscopy of brain tissue. *J. Vis. Exp.* **53**, e2588.

Kolotuev, I. (2014). Positional correlative anatomy of invertebrate model organisms increases efficiency of TEM data production. *Microsc. Microanal.* **20**, 1392-1403.

Kolotuev, I., Schwab, Y. and Labouesse, M. (2010). A precise and rapid mapping protocol for correlative light and electron microscopy of small invertebrate organisms. *Biol. Cell* **102**, 121-132.

Kolotuev, I., Hyenne, V., Schwab, Y., Rodriguez, D. and Labouesse, M. (2013). A pathway for unicellular tube extension depending on the lymphatic vessel determinant Prox1 and on osmoregulation. *Nat. Cell Biol.* **15**, 157-168.

Kopek, B. G., Paez-Segala, M. G., Shtengel, G., Sochacki, K. A., Sun, M. G., Wang, Y., Xu, C. S., van Engelenburg, S. B., Taraska, J. W., Looger, L. L. et al. (2017). Diverse protocols for correlative super-resolution fluorescence imaging and electron microscopy of chemically fixed samples. *Nat. Protoc.* **12**, 916-946.

Kremer, J. R., Mastronarde, D. N. and McIntosh, J. R. (1996). Computer visualization of three-dimensional image data using IMOD. *J. Struct. Biol.* **116**, 71-76.

Kremer, A., Lippens, S., Bartunkova, S., Asselbergh, B., Blanpain, C., Fendrych, M., Goossens, A., Holt, M., Janssens, S., Krols, M. et al. (2015). Developing 3D SEM in a broad biological context. *J. Microsc.* **259**, 80-96.

Kukulski, W., Schorb, M., Welsch, S., Picco, A., Kaksonen, M. and Briggs, J. A. G. (2011). Correlated fluorescence and 3D electron microscopy with high sensitivity and spatial precision. *J. Cell Biol.* **192**, 111-119.

Lee, W.-C. A., Bonin, V., Reed, M., Graham, B. J., Hood, G., Glattfelder, K. and Reid, R. C. (2016). Anatomy and function of an excitatory network in the visual cortex. *Nature* **532**, 370-374.

Li, X., Ji, G., Chen, X., Ding, W., Sun, L., Xu, W., Han, H. and Sun, F. (2017). Large scale three-dimensional reconstruction of an entire Caenorhabditis elegans larva using AutoCUTS-SEM. *J. Struct. Biol.* **200**, 87-96.

Loussert Fonta, C. and Humbel, B. M. (2015). Correlative microscopy. *Arch. Biochem. Biophys.* **581**, 98-110.

Loyer, N., Kolotuev, I., Pinot, M. and Le Borgne, R. (2015). Drosophila E-cadherin is required for the maintenance of ring canals anchoring to mechanically withstand tissue growth. *Proc. Natl. Acad. Sci. USA* **112**, 12717-12722.

Lucas, M. S., Günthert, M., Gasser, P., Lucas, F. and Wepf, R. (2012). Bridging microscopes: 3D correlative light and scanning electron microscopy of complex biological structures. *Methods Cell Biol.* **111**, 325-356.

Lucas, M. S., Guenthert, M., Gasser, P., Lucas, F. and Wepf, R. (2014). Correlative 3D imaging: CLSM and FIB-SEM tomography using high-pressure frozen, freeze-substituted biological samples. *Methods Mol. Biol.* **1117**, 593-616.

Maco, B., Holtmaat, A., Cantoni, M., Kreshuk, A., Straehle, C. N., Hamprecht, F. A. and Knott, G. W. (2013). Correlative in vivo 2 photon and focused ion beam scanning electron microscopy of cortical neurons. *PLoS ONE* **8**, e57405.

Markert, S. M., Britz, S., Proppert, S., Lang, M., Witvliet, D., Mulcahy, B., Sauer, M., Zhen, M., Bessereau, J.-L. and Stigloher, C. (2016). Filling the gap: adding super-resolution to array tomography for correlated ultrastructural and molecular identification of electrical synapses at the C. elegans connectome. *Neurophotonics* **3**, 041802.

McDonald, K. L. (2014). Rapid embedding methods into epoxy and LR White resins for morphological and immunological analysis of cryofixed biological specimens. *Microsc. Microanal.* **20**, 152-163.

McLaughlin, J. M. and Bratu, D. P. (2015). Drosophila melanogaster oogenesis: an overview. *Methods Mol. Biol.* **1328**, 1-20.

McLean, P. F. and Cooley, L. (2013). Protein equilibration through somatic ring canals in Drosophila. *Science* **340**, 1445-1447.

Micheva, K. D. and Smith, S. J. (2007). Array tomography: a new tool for imaging the molecular architecture and ultrastructure of neural circuits. *Neuron* **55**, 25-36.

Micheva, K. D., Busse, B., Weiler, N. C., O'Rourke, N. and Smith, S. J. (2010). Single-synapse analysis of a diverse synapse population: proteomic imaging methods and markers. *Neuron* **68**, 639-653.

Muller-Reichert, T. and Verkade, P. (2014). Preface. Correlative light and electron microscopy II. *Methods Cell Biol.* **124**, xvii-xviii.

Nicolle, O., Burel, A., Griffiths, G., Michaux, G. and Kolotuev, I. (2015). Adaptation of cryo-sectioning for IEM labeling of asymmetric samples: a study using Caenorhabditis elegans. *Traffic* **16**, 893-905.

Nixon, S. J., Webb, R. I., Floetenmeyer, M., Schieber, N., Lo, H. P. and Parton, R. G. (2009). A single method for cryofixation and correlative light, electron microscopy and tomography of zebrafish embryos. *Traffic* **10**, 131-136.

Noske, A. B., Costin, A. J., Morgan, G. P. and Marsh, B. J. (2008). Expedited approaches to whole cell electron tomography and organelle mark-up in situ in high-pressure frozen pancreatic islets. *J. Struct. Biol.* **161**, 298-313.

Oberti, D., Kirschmann, M. A. and Hahnloser, R. H. R. (2011). Projection neuron circuits resolved using correlative array tomography. *Front. Neurosci.* **5**, 50.

Paez-Segala, M. G., Sun, M. G., Shtengel, G., Viswanathan, S., Baird, M. A., Macklin, J. J., Patel, R., Allen, J. R., Howe, E. S., Piszczek, G. et al. (2015). Fixation-resistant photoactivatable fluorescent proteins for CLEM. *Nat. Methods* **12**, 215-218, 214 p following 218.

Paul-Gilloteaux, P., Heiligenstein, X., Belle, M., Domart, M.-C., Larijani, B., Collinson, L., Raposo, G. and Salamero, J. (2017). eC-CLEM: flexible multidimensional registration software for correlative microscopies. *Nat. Methods* **14**, 102-103.

Peddie, C. J., Blight, K., Wilson, E., Melia, C., Marrison, J., Carzaniga, R., Domart, M.-C., O'Toole, P., Larijani, B. and Collinson, L. M. (2014). Correlative and integrated light and electron microscopy of in-resin GFP fluorescence, used to localise diacylglycerol in mammalian cells. *Ultramicroscopy* **143**, 3-14.

Pluk, H., Stokes, D. J., Lich, B., Wieringa, B. and Fransen, J. (2009). Advantages of indium-tin oxide-coated glass slides in correlative scanning electron microscopy applications of uncoated cultured cells. *J. Microsc.* **233**, 353-363.

Robinson, D. N., Cant, K. and Cooley, L. (1994). Morphogenesis of Drosophila ovarian ring canals. *Development* **120**, 2015-2025.

Saalfeld, S., Fetter, R., Cardona, A. and Tomancak, P. (2012). Elastic volume reconstruction from series of ultra-thin microscopy sections. *Nat. Methods* **9**, 717-720.

Schindelin, J., Arganda-Carreras, I., Frise, E., Kaynig, V., Longair, M., Pietzsch, T., Preibisch, S., Rueden, C., Saalfeld, S., Schmid, B. et al. (2012). Fiji: an open-source platform for biological-image analysis. *Nat. Methods* **9**, 676-682.

Schwarz, H. and Humbel, B. M. (2014). Correlative light and electron microscopy using immunolabeled sections. *Methods Mol. Biol.* **1117**, 559-592.

Starborg, T., Kalson, N. S., Lu, Y., Mironov, A., Cootes, T. F., Holmes, D. F. and Kadler, K. E. (2013). Using transmission electron microscopy and 3View to determine collagen fibril size and three-dimensional organization. *Nat. Protoc.* **8**, 1433-1448.

Sundaram, M. V. and Buechner, M. (2016). The Caenorhabditis elegans excretory system: a model for tubulogenesis, cell fate specification, and plasticity. *Genetics* **203**, 35-63.

Titze, B. and Genoud, C. (2016). Volume scanning electron microscopy for imaging biological ultrastructure. *Biol. Cell* **108**, 307-323.

Wacker, I. and Schroeder, R. R. (2013). Array tomography. *J. Microsc.* **252**, 93-99.

Wacker, I., Spomer, W., Hofmann, A., Thaler, M., Hillmer, S., Gengenbach, U. and Schröder, R. R. (2016). Hierarchical imaging: a new concept for targeted imaging of large volumes from cells to tissues. *BMC Cell Biol.* **17**, 38.

Watanabe, S., Punge, A., Hollopeter, G., Willig, K. I., Hobson, R. J., Davis, M. W., Hell, S. W. and Jorgensen, E. M. (2011). Protein localization in electron micrographs using fluorescence nanoscopy. *Nat. Methods* **8**, 80-84.

White, J. G., Southgate, E., Thomson, J. N. and Brenner, S. (1986). The structure of the nervous system of the nematode Caenorhabditis elegans. *Philos. Trans. R. Soc. Lond. B Biol. Sci.* **314**, 1-340.

Supplementary Figure 1

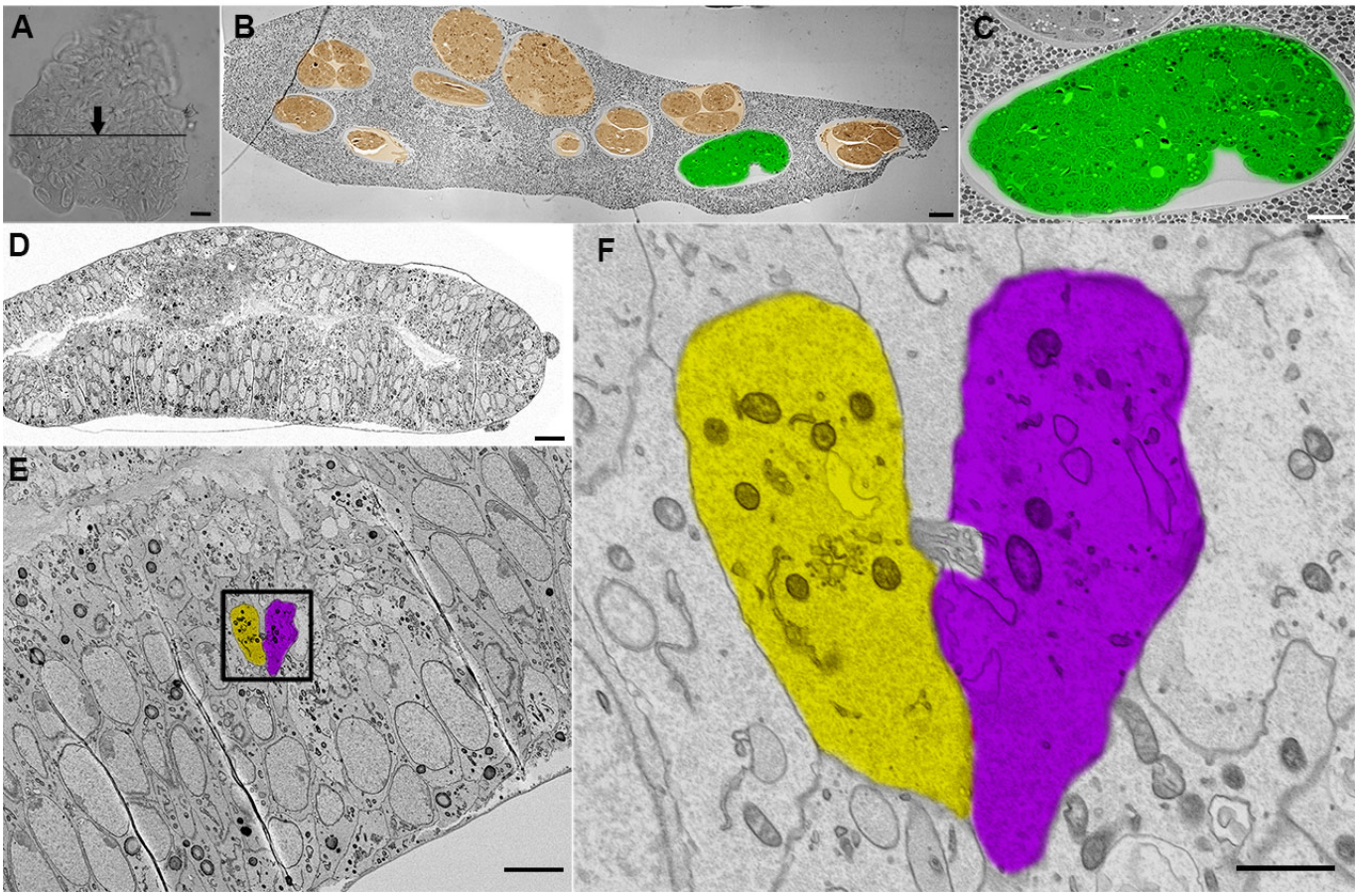

Figure S1. Examples of AT-assisted analysis of different complex samples

A. "Blind screening" of *C. elegans* embryos: A resin block containing a pellet of mixed stage embryos randomly sectioned through the area designated by the black line. Scale bar, 50 µm.

B. Low-magnification SEM-BSE image of a section from Panel A (black line). Embryos at various stages are pseudo-colored in orange, and a 1.2-fold stage embryo in the desired orientation is colored in green. Scale bar, 10 µm.

C. High-magnification image of the embryo of interest (Panel B). Rapid AT screening will provide sufficient embryos at the desired stage for the operator to choose the desired orientation, based on previous knowledge of the anatomy of the specimen. Thus, sample orientation is unnecessary. Scale bar, 5 µm.

D. SEM section through a *Drosophila* larval wing disc. Scale bar, 10 µm.

E. High magnification of epithelial cells within the wing disc (Panel D). Cell division events are frequently studied in the *Drosophila* wing disc in fixed tissue processed for TEM. Locating the event of cell abscission and retrieving the complete volume of both dividing cells is technically challenging. Quick screening of multiple regions in numerous rows of sections facilitates this operation, allowing the timely location of the desired area. Scale bar, 2 µm.

F. High magnification view (Panel E): two cells (yellow and purple) at the end of cell division, in telophase, with the cellular bridge still connecting both cells. Scale bar, 1 µm.

Supplementary Figure 2

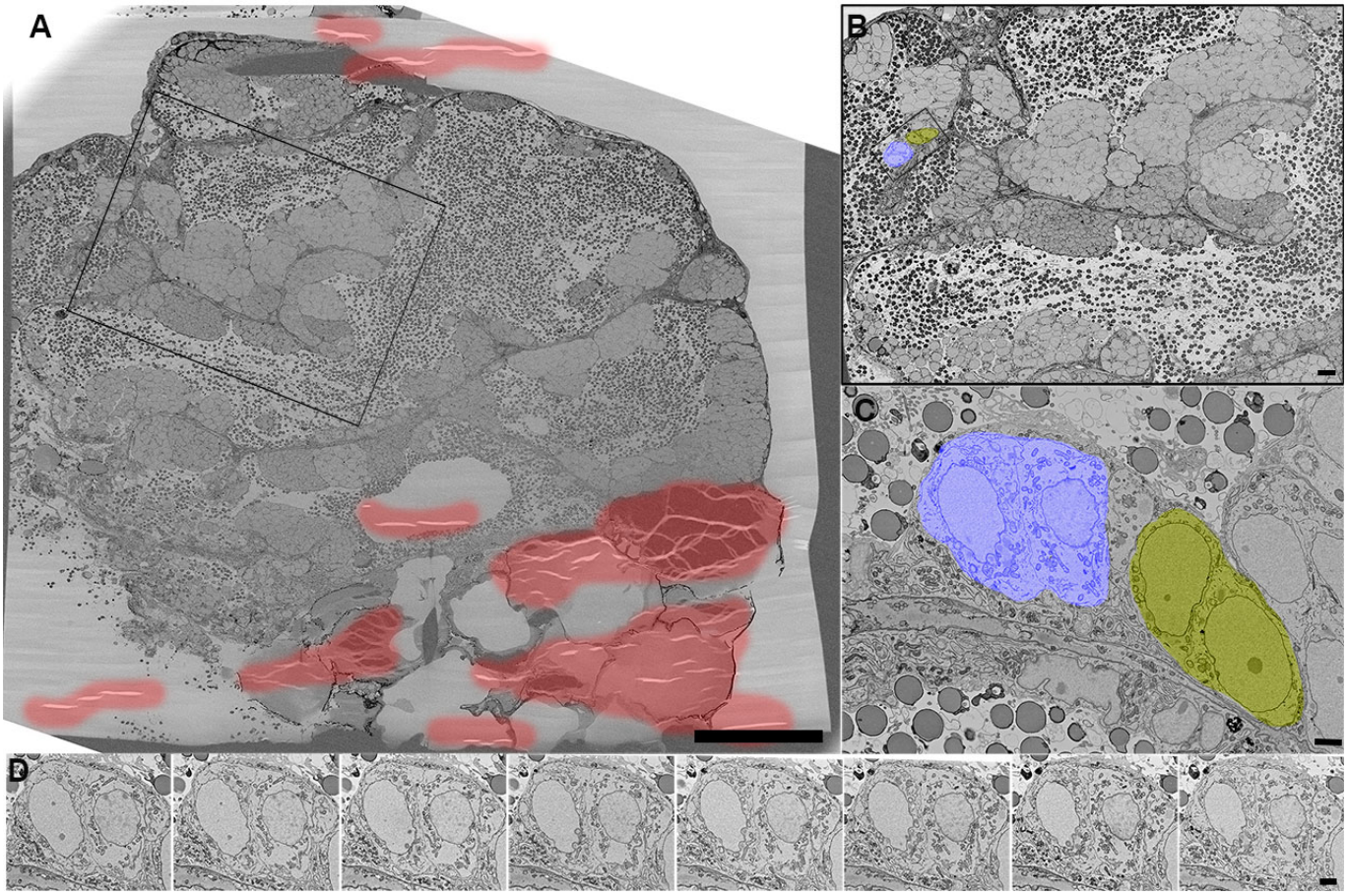

Figure S2. Examples of AT-assisted analysis of different complex samples

A. Low magnification view on a section an SEM image of a cross-section through a zebrafish testis. The regions containing the folds/microfolds are highlighted in red. Scale bar 100 µm.

B. Higher magnification on the global area of interest (black rectangle in Panel A) that contains no wrinkles. The structure is composed of cell clusters (cysts) at various stages of cell division. The mother cells that initiate such clusters by undergoing multiple rounds of cell division are randomly scattered throughout the spermatheca. Our AT approach with “blind” sectioning greatly facilitates locating the mother cells compared with standard sectional analysis. Black box encircles a potential ROI. Scale bar, 10 µm.

C. Close-up of two pairs of precursor cells highlighted in blue and in yellow (Box in Panel G). After a single section containing the ROI has been identified by “horizontal” screening (Figure 4C), the sections sequentially upstream and downstream of the initially identified section (i.e., “vertical”) within the same ribbon of consecutive sections can be analyzed. Scale bar, 2 µm.

D. A sequence of serial images obtained from the blue area (Panel G). None of the sections was affected either by the folds or the microfolds. Scale bar 2 µm.

Supplementary Figure 3

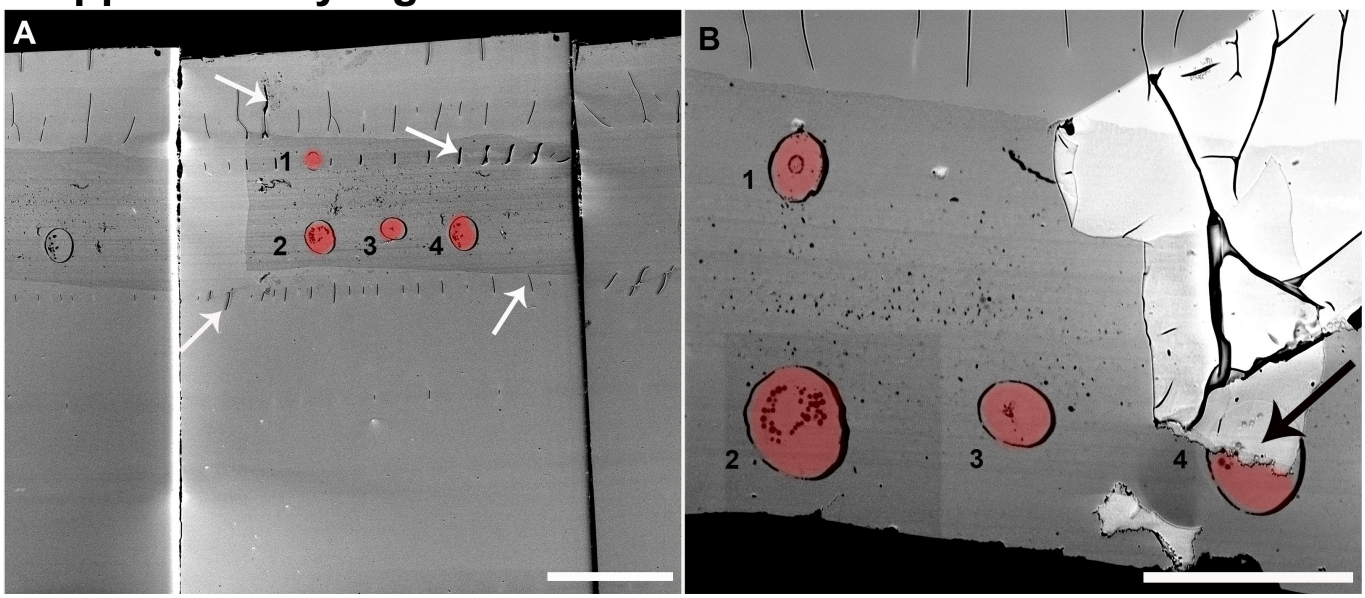

Figure S3. An example of the folds and micro folds on sections

A. An overview of several ribbons of consecutive sections on a wafer. Four *C. elegans* larvae, randomly cut through the body are shown. Arrows point to some microfolds. Scale bar 100 µm.

B. An example of a severe damage on section. Part of the resin from another section has landed on the adjacent section, partially ruining it (arrow). Scale bar 50 µm.

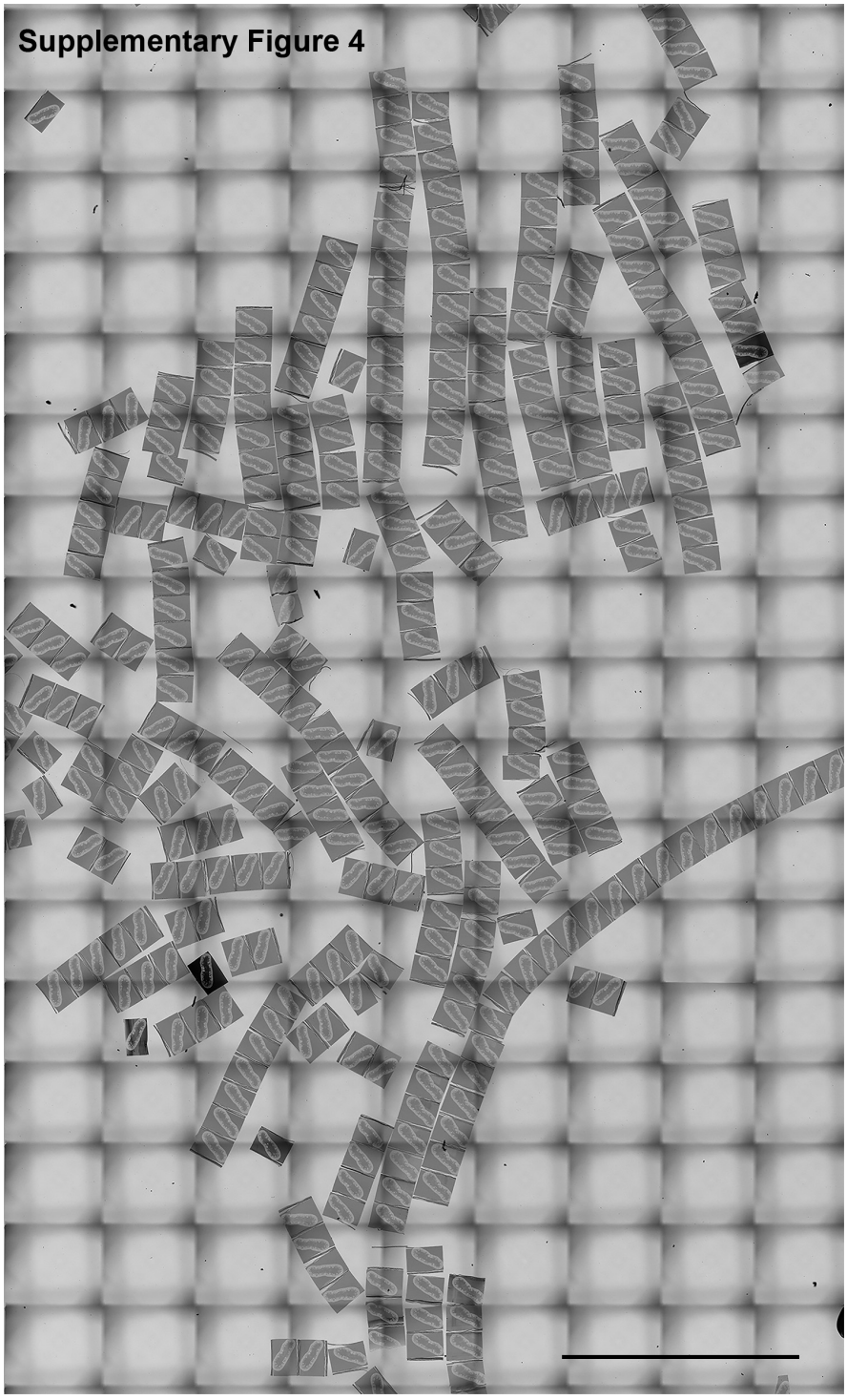

Figure S4. Scattered sections collected on wafer in a random orientation

Drosophila gut sections transferred on the wafer. Multiple low magnification tiles stitched together. An example of particularly unsuccessful sectioning and arrays alignment. Sections are scattered in all directions and even in this severe case there are few to none folds on sections. The image can be zoomed in to see the details. Scale bar 500 µm.

Supplementary Movies

Movie 1. Sectioning and on-wafer transfer of the arrays using the modified diamond knife with the modified basin. There are several key steps in this procedure:

1. Sectioning. The time required for sectioning depends on the desired number of sections and the speed of sectioning. We used a rate of 0.8-1.0 μm/sec.

2. Alignment of ribbons of consecutive sections. During the first step, one or several ribbons can be generated. Multiple ribbons can be arranged side by side using gentle movements of an eyelash attached to a thin stick.

3. Water draining. Water retraction can be achieved by active aspiration through the syringe and by passive dripping through the plastic catheter. The entire procedure takes a couple of minutes at the most.

4. Readjustment of ribbons. While draining the water from the basin, the aligned ribbons often become misaligned. While water remains on the surface of the wafer, we can readjust the ribbons until the surface starts to dry.

5. Gradual evaporation of water from the surface of the wafer. We consider this step to be critical to avoid folds in the sections. The visual zoom-in on a drying portion of the ribbon illustrates this concept well. The length of time for drying will largely depend on the size of the surface area and the surrounding environmental conditions. In practice, drying takes 10 to 30 minutes for a wafer of 2x4 cm.

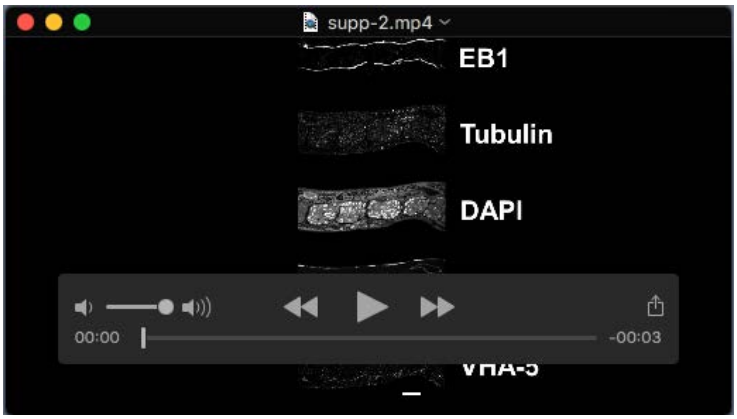

Movie 2. Alignment of the sequences of the labeled sections presented in Figure 2.

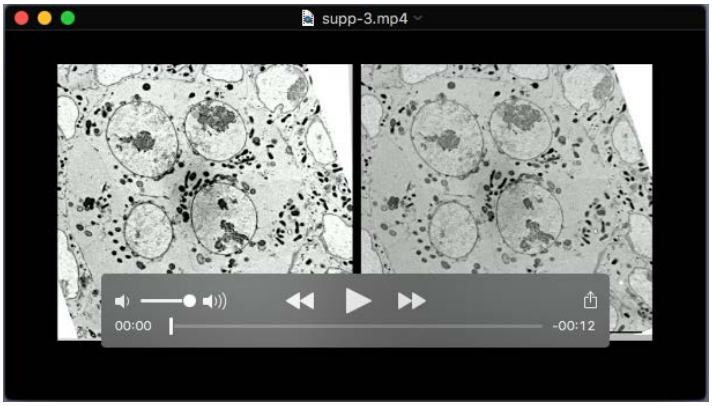

Movie 3. Alignment of multiple SEM-BSE images of sections through *Drosophila* ovarian chamber. All ring canals are pseudo-colored in orange with the selected ring in magenta. Side by side representation of the on-surface tracking (left) and a 3D ring canals rendering model (right).

Movie 4. Close-up of a ring canal from the dataset presented in the Movie 3, colored in magenta, captures with using higher-resolution SEM-BSE acquisition parameters.

Movie 5. Modeling and rendering data set of multiple SEM-BSE images of sections through a *Drosophila* ovarian chamber. An IMOD reconstruction of 80 sections featuring cells labeled in various colors as well as their interactions, and the connections through the ring canals (yellow).

Macro

```
macro register_tomo_fluo{
	Dialog.create("Register tomo fluo");
	Dialog.addChoice("Macro", newArray("Split Stack", "Register Reference", "Apply
transformation"));
	Dialog.show();
	macroChoice = Dialog.getChoice;

	if (macroChoice == "Split Stack"){

		// params
		Dialog.create("Channel number");
		Dialog.addNumber("Channel number", 3);
		Dialog.show();
		channelNumber = Dialog.getNumber;

		// input image
		var inputImageID = getImageID();
		var inputImageTitle = getTitle();
		print("tomo");getDimensions(width, height, channels, slices, frames);print("tomo1");
		var slicesNb = slices;
		var imageMaxSize = maxOf(width, height);

		// parameters values
		var outputDir = getDirectory("Choose a Directory");

		// split the channels to individual files
		for(c =1 ; c <= channelNumber ; c++){
			File.makeDirectory(outputDir + "C" + c);
		}

		splitStackToImages(channelNumber);
	}
	else if(macroChoice == "Register Reference"){

		// get parameters
		Dialog.create("Register tomo fluo");
		Dialog.addChoice("Reference channel", newArray("C1", "C2", "C3", "C4", "C5", "C6"));
		Dialog.addNumber("Registered Iage Size", 1024);
		Dialog.show();
		var referenceChannel = Dialog.getChoice;
		var imageMaxSize = Dialog.getNumber;
		var outputDir = getDirectory("Select the Directory containing the Cx input images
folder");


		// register reference stack
		File.makeDirectory(outputDir + "reg_C1");
		File.makeDirectory(outputDir + "reg_C2");
		File.makeDirectory(outputDir + "reg_C3");
		File.makeDirectory(outputDir + "reg_C4");
		File.makeDirectory(outputDir + "reg_C5");
```

```
		File.makeDirectory(outputDir + "reg_C6");
		File.makeDirectory(outputDir + "reg_transform");
		register_reference();
	}
	else if(macroChoice == "Apply transformation"){

		var outputDir = getDirectory("Choose a Directory");
		applyTranformation();
	}
}

function splitStackToImages(channelNumber){

	//run("Stack to Hyperstack...", "order=xyczt(default) channels=3 slices="+slicesNb/3+" frames=1
display=Color");
	run("Split Channels");

	for (c = 1 ; c <=channelNumber ; c++){
		selectWindow("C"+c+"-" + inputImageTitle);
		run("Image Sequence... ", "format=TIFF save=["+outputDir + "C"+c+"\\C"+c+"-
0000.tif]");
	}
}

function register_reference(){

	run("Register Virtual Stack Slices", "source="+outputDir+referenceChannel +
	   " output="+outputDir+"reg_"+referenceChannel +" feature=Rigid
registration=[Rigid		-- translate + rotate		]" +
	   " advanced save initial_gaussian_blur=1.60 steps_per_scale_octave=3
minimum_image_size=64 maximum_image_size="+imageMaxSize+" "+
	   " feature_descriptor_size=8 feature_descriptor_orientation_bins=8
closest/next_closest_ratio=0.92 maximal_alignment_error=25 "+
	   " inlier_ratio=0.05 feature_extraction_model=Rigid registration_model=[Rigid		--
translate + rotate		] interpolate");

}

function applyTranformation(){

	for(c = 1 ; c <=6 ; c++ ){
		channel = "C"+c;
		args = "source="+outputDir + channel+" output="+outputDir+"reg_"+channel+"
transforms="+outputDir+"reg_transform"+" interpolate";
		run("Transform Virtual Stack Slices", args);
	}
	run("Merge Channels...", "c1=[Registered C1] c2=[Registered C2] c3=[Registered C3]
c4=[Registered C4] c5=[Registered C5] c6=[Registered C6] create");
	Stack.setDisplayMode("color");
	saveAs("TIFF", outputDir + "reg_stack.tif");
}
```